Article

Plasma membrane topography governs the 3D dynamic localization of IgM B cell antigen receptor clusters

Deniz Saltukoglu[1,2] (iD), Bugra Özdemir[2,3,†] (iD), Michael Holtmannspötter[4] (iD), Ralf Reski[2,3] (iD), Jacob Piehler[4] (iD), Rainer Kurre[4] (iD) & Michael Reth[1,2,*] (iD)

Abstract

B lymphocytes recognize bacterial or viral antigens via different classes of the B cell antigen receptor (BCR). Protrusive structures termed microvilli cover lymphocyte surfaces, and are thought to perform sensory functions in screening antigen-bearing surfaces. Here, we have used lattice light-sheet microscopy in combination with tailored custom-built 4D image analysis to study the cell-surface topography of B cells of the Ramos Burkitt's Lymphoma line and the spatiotemporal organization of the IgM-BCR. Ramos B-cell surfaces were found to form dynamic networks of elevated ridges bridging individual microvilli. A fraction of membrane-localized IgM-BCR was found in clusters, which were mainly associated with the ridges and the microvilli. The dynamic ridge-network organization and the IgM-BCR cluster mobility were linked, and both were controlled by Arp2/3 complex activity. Our results suggest that dynamic topographical features of the cell-surface govern the localization and transport of IgM-BCR clusters to facilitate antigen screening by B cells.

Introduction

Clonal selection of B lymphocytes is initiated when they recognize cognate antigens via their B cell antigen receptor (BCR) within secondary lymphoid organs (Roozendaal *et al*, 2009; Cyster, 2010; Gonzalez *et al*, 2011; Kuka & Iannacone, 2018). In these organs, B cells actively survey specialized antigen-bearing cells (Wykes *et al*, 1998; Qi *et al*, 2006; Carrasco & Batista, 2007; Junt *et al*, 2007; Phan *et al*, 2007; Cinamon *et al*, 2008; Roozendaal *et al*, 2008; Suzuki *et al*, 2009; Cai *et al*, 2017). Antigen surveillance and sensing are thought to be facilitated by actin-based lymphocyte protrusions called microvilli that cover the cell surface (Majstoravich *et al*, 2004; Sage *et al*, 2012; Cai *et al*, 2017; Orbach & Su, 2020). Genetic studies show that components of the actin cytoskeleton play a major role in both the regulation and activation of different BCR classes and that mutations in cytoskeletal genes can cause auto-immune diseases and/or immunodeficiency (Thrasher, 2009; Lanzi *et al*, 2012; Moshous *et al*, 2013; Keppler *et al*, 2018; Bouafia *et al*, 2019; Rey-Suarez *et al*, 2020). The IgM- and IgD-class BCRs on naïve B cells form separate clusters on the B cell surface (Maity *et al*, 2015). IgM- and IgD-BCR functionally connect to different transmembrane proteins within their proximity, suggesting that the B cell plasma membrane is compartmentalized (Kläsener *et al*, 2014; Becker *et al*, 2017), similar to what has been reported in T cells (Lillemeier *et al*, 2010; Roh *et al*, 2015). Cell surface topography in conjunction with the actin cytoskeleton has the potential to contribute to the compartmentalization of cell surface molecules. Topography-dependent distribution of immune-related cell surface proteins is a topic of growing interest and has implications for receptor silencing and immune cell surveillance strategies (Cai *et al*, 2017; Fernandes *et al*, 2019; Orbach & Su, 2020; Franke *et al*, 2022). Live cell total internal reflection fluorescence (TIRF) microscopy studies suggest that cell surface dynamics of the IgM-BCR is linked to the underlying actin cytoskeleton (Treanor *et al*, 2010; Mattila *et al*, 2013, 2016; Tolar, 2017; Rey-Suarez *et al*, 2020). However, 3D topography-dependent localization of IgM-BCR is difficult to address with TIRF microscopy because imaging is limited to a single plane, and the requirement to spread B cells on substrates leads to the flattening of protrusive structures such as the microvilli. Variations of the TIRF technique such as variable angle-TIRF microscopy performed on fixed T cells demonstrated that the T cell receptor (TCR) and CCR7 accumulate at the tips of microvilli (Jung *et al*, 2016; Ghosh *et al*, 2021). An

1   Department of Molecular Immunology, Biology III, Faculty of Biology, University of Freiburg, Freiburg, Germany
2   Signaling Research Centers CIBSS and BIOSS, University of Freiburg, Freiburg, Germany
3   Plant Biotechnology, Faculty of Biology, University of Freiburg, Freiburg, Germany
4   Department of Biology/Chemistry and Center for Cellular Nanoanalytics, Osnabrück University, Osnabrück, Germany
    *Corresponding author. Tel: +49-761-2032868; E-mail: michael.reth@bioss.uni-freiburg.de
    †Present address: Euro-BioImaging, European Molecular Biology Laboratory (EMBL), Heidelberg, Germany

improved substrate coating to keep T cell surface protrusions intact in living cells and application of three-dimensional (3D) single-molecule localization microscopy (SMLM) at the cell-substrate interface showed that membrane protrusions segregate CD4 from the transmembrane phosphatase CD45 (Franke *et al*, 2022). With expansion microscopy, it was demonstrated that CD45 is excluded from microvilli tips in T and B cells (Jung *et al*, 2021).

To understand IgM-BCR plasma membrane localization in the context of dynamic 3D surface topography, we have performed dual color lattice light sheet microscopy (LLSM) of IgM-BCR and a plasma membrane marker on cultured Burkitt's lymphoma Ramos B cells. LLSM with its ultra-thin light-sheets allows for high-speed 3D imaging with lowest phototoxicity and photobleaching (Chen *et al*, 2014). It provides almost aberration-free, diffraction-limited resolution with highest sensitivity and unmatched temporal resolution. These features make LLSM an efficient tool to study 3D surface dynamics. Quantification of cell surface intensity distributions in light sheet microscopy has previously been performed for PIP_2, K-ras and septins (Driscoll *et al*, 2019; Weems *et al*, 2021). In this work, we developed dedicated image analysis methods to correlate receptor localization with cell surface topography. We show that IgM-BCR forms clusters on the unperturbed 3D surface. We uncover that the B cell surface is patterned by an elevated ridge network on which microvilli emerge. IgM-BCR clusters localize to these protrusive structures and couple with their dynamics via the Arp2/3 complex. Moreover, the localization of IgM-BCR clusters to cellular protrusions are governed by factors upstream of the actin and microtubule cytoskeletons. Our findings imply a role for dynamic surface topography in functional BCR localization to facilitate antigen surveillance.

Results

The IgM-BCR is clustered on the Ramos B cell surface

For cell surface-selective photostable fluorescence labeling of the antigen receptor, we fused 4-hydroxy-3-iodo-5-nitrophenylacetyl (NIP)-specific IgM-BCR to an N-terminal SNAP-tag (SNAP-IgM-BCR). An external SNAP-tag labeling strategy was chosen to avoid signals from organelle-associated IgM-BCR. We retrovirally expressed SNAP-IgM-BCR in heavy and light chain gene-knockout (H/L-KO) Ramos B cells (He *et al*, 2018) along with EGFP carrying the 14 most C-terminal amino acid sequence including the farnesylated CaaX motif of the K-ras gene to visualize the plasma membrane (Fig EV1A and B). This EGFP-CaaX construct was well-expressed in cells and produced a high contrast between the plasma membrane and cytosol for efficient cell surface segmentation. To assess the distribution of another receptor family in comparison, we used an N-terminally tagged CD40 (SNAP-CD40). We confirmed SNAP-IgM-BCR's uncompromised signaling competence by activation with antigen (Fig EV1C and D). After cell surface labeling of the SNAP-tag, Matrigel-embedded Ramos B cells were imaged by LLSM in two channels (EGFP, DY549P1) with a speed of 2.5 s per volume. To limit the analysis of IgM-BCR and CD40 molecules to the plasma membrane, we created cell surface masks by segmenting the EGFP-CaaX volumes (Figs 1A and EV1E). 3D segmentation per time-frame was performed via a modification of nnU-Net (Isensee *et al*, 2021) using self-generated ground truth. To faithfully extract the surface topography and microvilli protrusions, the model was trained to be sensitive to fine details (Movie EV1).

Visual inspection of the EGFP-CaaX, SNAP-IgM-BCR and SNAP-CD40 signals in cross-sectional slices and surface-masked volumes showed that these proteins are differentially distributed on the plasma membrane (Fig 1B and C, Movie EV2). Compared with EGFP-CaaX and SNAP-CD40, SNAP-IgM-BCRs accumulated into dot-like, high-contrast structures. To quantify this effect, we developed a cluster segmentation method based on local intensity contrast in 3D image data. This method extracted distinct clusters of IgM-BCR (Fig 1D and E, Movie EV3). Along with the cluster segmentation, we proposed a metric (namely, "granularity") that roughly quantifies the accumulation of the signal in clusters. A granularity score of 0 indicates signal accumulation in the form of lines or cell surface patches, whereas 1 indicates perfect granules. After applying our cluster segmentation method to different classes of images, significantly higher granularity scores were obtained for IgM-BCR compared with EGFP-CaaX and SNAP-CD40 (Fig 1D and E, Movie EV3). In addition to granularity, we also quantified other features to understand whether the IgM signal is enriched within the segmented clusters. We found that the total signal within the segmented IgM-BCR clusters amounted to 22% of the surface-masked total receptor signal with a 2.1-fold increase in average

---

Figure 1. Distribution of SNAP-IgM-BCR and SNAP-CD40 on the B cell surface.

A 3D image of an EGFP-CaaX-expressing Ramos B cell embedded in Matrigel (left), segmentation of the inner dome (center) using our own script based on Watershed segmentation and segmentation of the cell surface (right) using an nnU-Net model that we trained based on our self-generated ground truth. Scale bar = 5 μm.

B Cross-sectional raw intensity images of a SNAP-IgM-BCR/EGFP-CaaX and a SNAP-CD40/EGFP-CaaX (only the DY549P1 channel shown) co-expressing Ramos B cell embedded within a Matrigel and imaged by LLSM in two channels (EGFP, DY549P1). Scale bar = 5 μm.

C Maximum intensity projection of surface-masked image stacks of the cells shown in (B).

D Cluster masks generated by a custom cluster detection algorithm based on local contrast.

E Cluster granularity score.

F Total voxel intensity in segmented clusters (Σ_{ci}) in comparison with the total voxel intensity within the cell surface mask (Σ_{ti}).

G Enrichment of intensity within the clusters. Average voxel intensity in segmented clusters (μ_{ci}) in comparison with the average voxel intensity of the non-clustered ("diffuse") signal within the cell surface mask (μ_{di}).

Data information: $n = 7$ (30-time frames/cell) for EGFP-CaaX and IgM-BCR from four independent experiments, $n = 3$ (50-time frames/cell) for CD40 from two independent experiments. Violin plot solid lines represent the median and dotted lines represent the quartiles in (E–G). Two-tailed, unpaired *t*-test was used in (E–G).

***$P < 0.001$, ****$P < 0.0001$. Comparison in (G) between IgM-BCR and CD40, $P = 0.0005$.

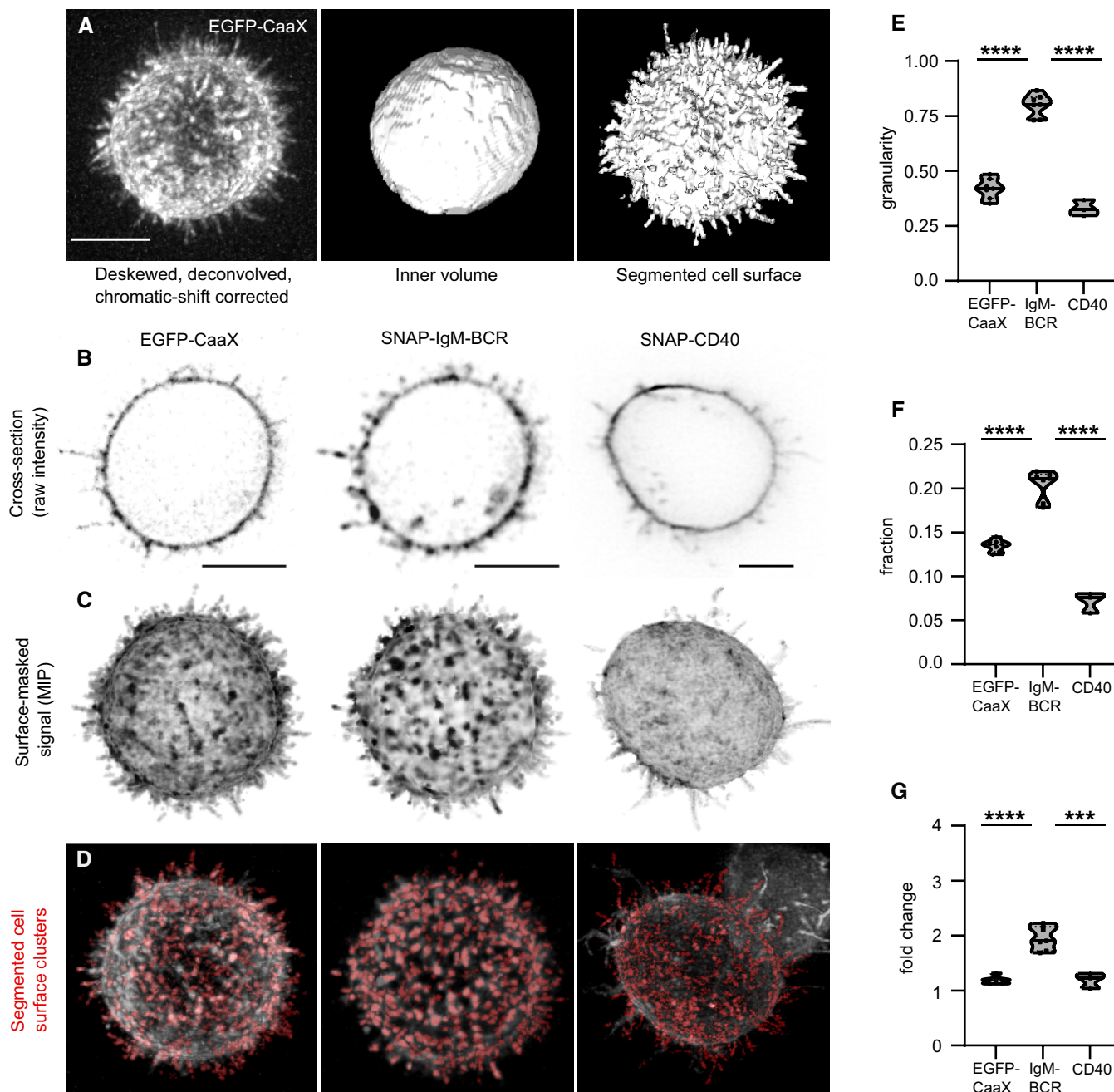Source data are available online for this figure.

Figure 1.

intensity (Fig 1F and G). This value was lower for EGFP-CaaX (14%) or CD40 (8%) with much less enrichment (1.2-fold) compared with IgM-BCR (Fig 1F and G). This quantification highlights that a substantial fraction of the IgM-BCR complexes on the plasma membrane of unstimulated Ramos B cells resides in clusters.

3D plasma membrane topography of Ramos B cells

To understand the cell surface topography of B cells in more detail, we transformed the surface mask into a triangular mesh and computed the micron-scale shapes using the shape index metric (Koenderink & van Doorn, 1992). The color-coded index shows that the B cell surface can be described by shallow invaginating cups (in yellow, labeled as "c") surrounded by saddles and elevated ridges (in blue, labeled as "r") in a repetitive way (Fig 2A and B). Thus, the whole Ramos B cell surface was classified into a pattern of positively- and negatively-curved micro-topographies. To analyze the organization of the ridge structure in more detail, we used a Hessian-based line filter to mask the curvilinear features on the raw intensity images of EGFP-CaaX (Fig EV1E). When the outcome (excluding the microvilli) was superimposed onto the EGFP-CaaX image, the extracted lines correlated with the elevated regions of the cell surface (Fig 2C). These elevated regions displayed higher EGFP-CaaX intensities, possibly because the ridges create opposing

membranes that are not resolved due to the diffraction limit of light and/or because they are preferred by the CaaX motif.

The extracted curviliniar features formed an interwoven network of polygonal patterns throughout the cell surface (Fig 2C and D). Importantly, all microvilli on the cell surface were extracted in connection with the ridges, confirming that microvilli are extensions on the elevated ridge network (Fig 2D). Network node analysis showed that most of the network nodes with or without a microvillus connection have a node degree of 3, implying simple branching in their formation (Fig 2E and F). In a smaller fraction (20%) of the nodes, the node degree was 4. Nodes with microvillus connections comprised 40% of all the extracted nodes on the skeleton (Fig 2G). In sum, the Hessian line extraction analysis showed that the elevated ridges and microvilli form an interconnected network that is topographically distinct from the rest of the Ramos B cell surface.

IgM-BCR clusters are enriched on the ridges and microvilli

After detailing the cell surface topography of Ramos B cells, we investigated whether IgM-BCR clusters are enriched at a particular surface structure. To do so, we compartmentalized the cell surface into distinct topographical features, namely, shallow invaginations (SI), ridges (R), nodes (N), microvilli shafts (MS) and microvilli tips (MT; Figs 3A and EV1E). Nodes corresponded to the sites where ridges and microvilli connect (microvillus roots) or to the sites where ridges laterally branch. Among the surface features, microvilli occupied the most volume, followed by shallow invaginations and ridges plus nodes (R + N; Fig EV2A).

To quantify cluster density at each surface feature (cluster count/feature volume), we represented each segmented IgM-BCR cluster by the coordinates of its centroid. Simulated random coordinates on the surface mask were distributed evenly across the five different surface features, showing that feature volume does not bias distribution (Fig 3D). In contrast, IgM-BCR clusters were least dense within the shallow invaginations and 1.8- and 4-fold enriched on the ridges and nodes, respectively (Fig 3B–D). Within the microvilli, cluster density was 1.5-fold enriched at the microvilli tips in comparison with microvilli shafts (Fig 3B–D).

To account for the extent of IgM-BCR accumulation in clusters at different surface features, we calculated the ratio of the mean IgM-BCR intensity within clusters (μ_{ci}) to the mean non-clustered ("diffuse") IgM-BCR intensity from the whole surface (μ_{di}). This ratio was highest at nodes with 2.5-fold increase and lowest at microvilli tips with a 1.2-fold increase (Fig 3E). Since our clustering algorithm detects local contrast, it can efficiently identify clusters within a high (ridge) and low (microvillus) diffuse intensity background (Fig EV2B–D).

In addition to this discrete analysis, we assessed the cluster distribution in a continuous manner with geodesic distance maps. We initiated these maps either from the ridge centerlines, the nodes or the microvilli tips and moved away from these initiation sites, sampling equal volumes (Fig 3F–H). Along the length of the microvillus geodesic distance map, IgM-BCR cluster density was highest at microvilli tips (Fig 3F). The IgM-BCR cluster density at the ridge and node geodesic distance maps also displayed a sharp decrease moving away from the initiation sites (Fig 3G and H). The decrease in CD40 cluster density was not as steep when moving away from ridge centerlines or nodes (Fig EV2F and G). However, CD40 density

was also highest at the microvilli tips within the microvilli (Fig EV2E). These analyses coherently substantiate that IgM-BCR clustering is localized in a patterned fashion and enriched at certain topographical features.

IgM-BCR mobility and ridge network dynamics are linked by Arp2/3 complex activity

Since the ridge network predominantly has a node-degree of 3, it is possible that branched actin polymerization mediated by the Arp2/3 complex is involved in its formation or dynamics. In cells treated with 100 μM of the Arp2/3 complex inhibitor CK-666 for 30 min, phalloidin staining did not detect significant decrease in polymerized cortical actin (Fig EV3A). In cells treated with CK-666 for 15–45 min, the ridge network could still be extracted and had a similar node-degree distribution as in untreated B cells (Fig EV3B). For visual inspection of the dynamics, we produced a sum projection of the skeletonized ridge network and microvilli along the time dimension in 15 consecutive frames, covering a window of 37.5 s. For a quantitative analysis of the dynamics of surface features and clusters, we propose the metric "staticity". Staticity is inversely correlated with the dynamics of the feature mask being analyzed. For the surface feature images, the staticity was calculated based on similarity scores using the "intersection over union" (IOU) method (Sanjaya *et al*, 2020) for consecutive pairs of time frames and was separately calculated for the skeletonized ridge and microvilli datasets. For cluster centroids the staticity was calculated from a staticity heatmap which was derived by correlating the datasets of cluster centroids with a 4D Gaussian kernel.

Untreated cells yielded blurred sum projection images of ridges and microvilli with low staticity scores, highlighting their dynamic nature (Fig 4A and D). In stark contrast, CK-666-treated cells displayed a frozen ridge network with high staticity scores. Different from what is reported for Jurkat T cells (Cai *et al*, 2017), the cumulative surface coverage of dynamic cell projections seemed to depend more on ridge dynamics rather than lateral microvilli movements in Ramos B cells (Fig EV3C). CK-666 effectively abolished the surface coverage mediated by the ridge network.

Interestingly, CK-666 treatment also strongly affected the clustering of IgM-BCR on the topographic landscape of the B cell. In comparison with untreated cells, Arp2/3 complex-inhibited cells displayed a higher IgM-BCR cluster density at ridges and nodes (Fig 4G and 3F). These clusters were brighter (Fig 4F) and arrested in mobility (Fig 4B, C and E, Movie EV4). In microvilli-assigned clusters (purple), arrested ones were mainly found at the roots of microvilli (Fig 4C). It is likely that these clusters occupy the highly curved joints at the ridge and microvillus intersection, suggesting that Arp2/3 complex function is required for IgM-BCR cluster mobility at this topographical region. During microvilli elongation, IgM-BCR entered the microvilli in a clustered form (Fig 4H, Movie EV5). IgM-BCR clusters dissipated and reformed, however, in a way that seemed to produce a forward movement towards the microvilli tips. In Arp2/3 complex-inhibited cells microvilli neither underwent elongation, nor de-novo formation (Movie EV4). Taken together, these data suggest that Arp2/3 complex-dependent cytoskeletal dynamics may promote the outward translocation of IgM-BCR clusters from the node pool to microvilli structures and link IgM-BCR cluster mobility to ridge and microvilli dynamics.
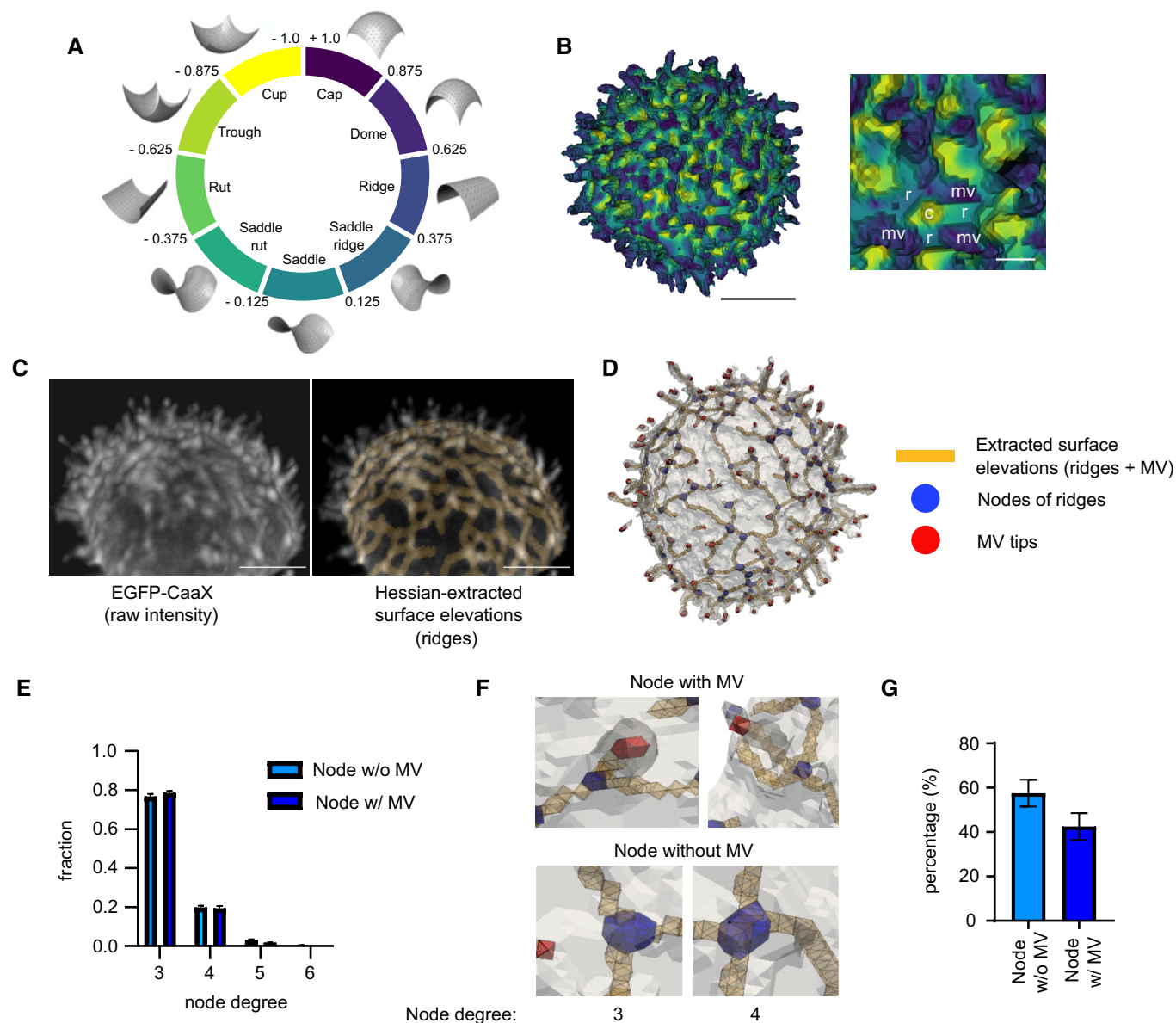
Figure 2. Identification of distinct morphological features on the B cell surface.

A   Color code of shapes according to the shape index metric.

B   Application of the shape index to the triangular surface mesh to highlight surface structures on a Matrigel-embedded Ramos B cell. The zoomed area reveals individual microvilli (mv) connecting to each other via positively curved ridges (r) and saddles, surrounding negatively curved cups (c) in a patterned way. Scale bar whole cell = 5 μm, inset = 1 μm.

C   Extraction of the ridge network on the B cell surface. Ridges were extracted from raw EGFP-CaaX images (left) using a Hessian-based algorithm and superimposed on the raw image (right). Scale bar = 5 μm.

D   The skeletonized ridge network including the microvilli protrusions superimposed on the mesh representation of the cell surface. The ridges, their connecting nodes and the microvilli tips are indicated by the yellow, blue and red color, respectively.

E   Node degree analysis of the skeletonized ridge network. Bars and error bars represent mean ± SD ($n = 4$, 30-time frames/cell).

F   Enlarged images of (D) displaying exemplary 3- and 4-degree nodes with or without microvillus association.

G   Percentage of the nodes without or with microvillus association. Bars and error bars represent mean ± SD ($n = 4$, 30-time frames/cell).

Source data are available online for this figure.

Antigen-induced micro-clusters associate with the ridge network

To find out how antigen stimulation affects IgM-BCR distribution on cell surface features, we used 50 ng/ml of 15mer NIP coupled to BSA (NIP-15-BSA) to stimulate the cells for 5–30 min. The binding of the cognate antigen led to the formation of the typical bright antigen-induced IgM-BCR micro-clusters (Ag-MC; Fig 5A). Using high-stringency cluster extraction (with local intensity fold change 3× or

higher), we found that these Ag-MC concentrated on the cell body but not on microvilli tips and microvilli shaft (Fig 5A and B). In terms of Ag-MC and ridge network dynamics, there were two profiles. In one profile, Ag-MC were immobilized on a frozen ridge network (Lower panel of Fig 5C–E) with higher cluster and ridge network staticity scores (Fig 5G and H). Interestingly, these cells displayed local ridge mobility at areas that lacked an Ag-MC (Fig 5F). In the second profile, Ag-MC underwent displacement on non-stabilized ridges (Upper panel of Fig 5C–E and G–I). Therefore, surface topography provides a platform for the anchoring and directional movement of Ag-MC.

IgM-BCR association with elevated topography is upstream of the actin and microtubule cytoskeletons

Next, we sought to find out how ridges and microvilli on the B cell surface are affected by the loss of the cortical actin cytoskeleton. Phalloidin staining demonstrated that the treatment of Ramos B cells with 2 µM Latrunculin A (LatA) for 30 min fully depolymerized the cortical actin cytoskeleton (Fig 6A) and a large part of the cell surface was smoothened (Fig 6B, D and I). Dynamic ridge network and microvilli were retracted, demonstrating that these structures are
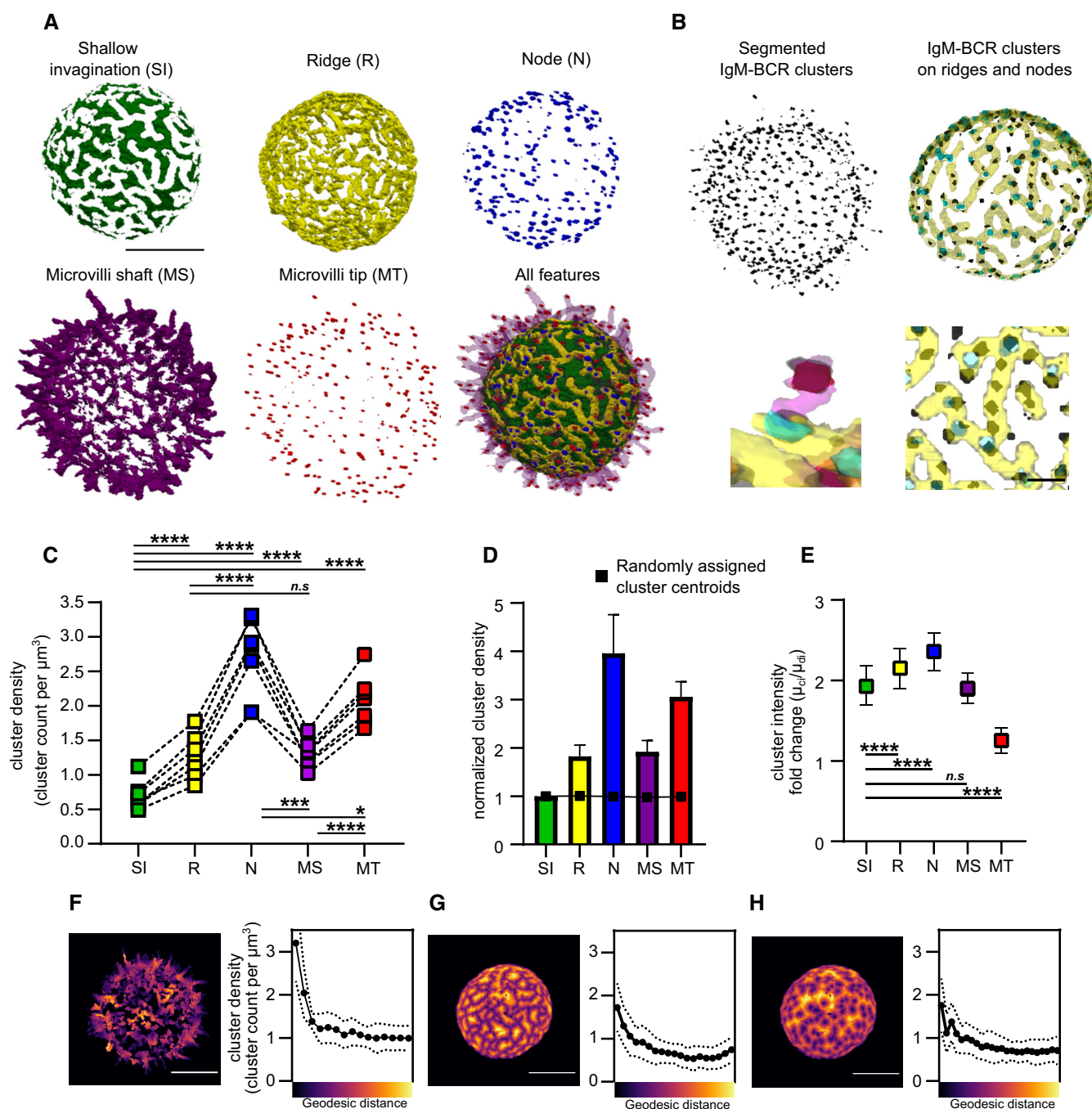

Figure 3.

Figure 3.   IgM-BCR clusters are enriched on ridges and microvilli.

A   Topographical features of the B cell surface. The cell body is separated from the microvilli (MV) protrusions using mathematical morphology. On the cell body, the ridge (R) network (yellow) is computed and its nodes (N; blue) are annotated. The remaining surface area is termed shallow invaginations (SI, dark green). Individual microvilli are split into their shaft (MS) and tip (MT, red) and all features are combined in one image. Scale bar = 5 μm.

B   Segmented IgM-BCR clusters (black) are superimposed onto the extracted surface features. Cluster-surface feature overlay reveals the accumulation of IgM-BCR clusters on ridges and their nodes. The zoomed-in microvillus displays a cluster density at its root (corresponding to a node) and tip. Scale bar inset = 1 μm.

C   Cluster density at surface features. IgM-BCR cluster density within different topographical features quantified as cluster count per surface feature volume.

D   Normalized cluster density. Comparison of mean cluster densities computed in (C) as normalized to the value of shallow invaginations. The black squares indicate the SI-normalized cluster density of randomly assigned cluster centroids on the cell surface. Bars and error bars represent mean ± SD.

E   IgM-BCR intensity enrichment within the segmented clusters at different surface features, calculated for the cells quantified in (C). Intensity enrichment was measured by dividing the average voxel intensity in the IgM-BCR clusters (μ_{ci}) by the average voxel intensity of the non-clustered IgM-BCR residing within the surface feature mask (μ_{di}). Data points and error bars represent mean ± SD.

F–H Continuous analysis of IgM-BCR cluster density using geodesic distance maps initiated from (F) microvilli tips towards microvilli roots, (G) centerline of ridges towards cell body surface, and (H) nodes towards cell body surface. Data points and the dotted lines represent mean ± SD. Scale bars = 5 μm.

Data information: *n* = 7 cells (30-time frames/cell) from four independent experiments were analyzed. Two-tailed, paired Student *t*-test was used in (C) and (E). **P* < 0.05, ***P* < 0.01, ****P* < 0.001, *****P* < 0.0001. Comparison in (C) between N and MS, *P* = 0.0003; between N and MT, *P* = 0.0145.
Source data are available online for this figure.

maintained by the actin cytoskeleton. However, LatA-treated cells displayed one large polarized protrusive region, which was static (Fig 6B, D and I, Movies EV6 and EV7) and some elongated or spot-like elevations, which could slide on the plasma membrane as a whole and merge with each other when in close vicinity (Fig 6C, Movie EV6). The large polarized protrusive structure upon LatA treatment formed immediately following treatment and contained polarized residual filamentous actin at early time points (Fig EV4A). However, the structure persisted after the whole actin cytoskeleton was depolymerized (Fig EV4A). Depolymerizing the microtubule cytoskeleton with 20 μM Nocodazole (Noc) for 30 min before LatA treatment abolished the formation of the polarized protrusive structure and led to enlarged, fully rounded cells (Fig EV4B). However, adding Noc to cells after 30 min of LatA incubation did not alter the cellular phenotype induced by only-LatA (Fig EV4C). Hence, LatA-induced polarized protrusions involve a guidance cue from the microtubule cytoskeleton but are maintained by factors other than microtubules or filamentous actin.

With LatA treatment, IgM-BCR clusters were not dispersed (Fig 6D, F and I). In smooth regions, as the topographical unevenness of the surface was compromised, the differences in the intensity distribution of EGFP-CaaX and IgM-BCR became more evident (Fig 6D and I, Movie EV7 – upper panel, Movie EV8). Segmented IgM-BCR

clusters in LatA-treated cells did not display a preference for smooth or elevated regions (Fig 6G). Although the increase in the staticity score was not significant, IgM-BCR clusters looked trapped within the elevated regions (Fig 6H, Movie EV7 - upper panel and Movie EV8). The non-significance is likely due to the fact that receptor clusters could move within the confines of elevations and elevations could themselves move on the cell surface. On the other hand, IgM-BCR clusters did not undergo entrapment and were mobile on the smooth regions (Fig 6H, Movie EV7 - upper panel and Movie EV8). Interestingly, the sum projection of cluster centroids (amounting to 37.5 s) that were associated with the smooth regions produced a localization map consisting of short linear trajectories and cluster-absent regions in a patterned way (Fig 6I). Sum projections taken iteratively at each time point demonstrated that this collective trajectory of mobile clusters on smooth regions seemed to form a network of polygonal patterns, surprisingly resembling the pattern framework of the ridges (Movie EV9 and Fig EV4D).

After antigen stimulation of LatA-treated Ramos B cells, Ag-MC were distinctively enriched on the large polarized protrusion and the elevated regions (Fig 6D, F and G, Movie EV7 - lower panel). This enrichment seemed to result at least partially from directional mobility of Ag-MC towards these regions (Fig 6E, Movie EV10), similar to what is observed in the formation of the immunological

Figure 4.   IgM-BCR cluster dynamics are linked with ridge network dynamics in an Arp2/3 complex-dependent manner.

A, B   Sum projections of the skeletonized ridge network and microvilli (A) and segmented IgM-BCR clusters (B) in an untreated and 100 μM CK-666-treated cell for 15 consecutive time frames amounting to 37.5 s. Scale bars = 5 μm.

C   Color coding of the segmented IgM-BCR clusters in (B) according to their assigned surface feature. Green clusters correspond to shallow invaginations (SI), yellow to ridge plus nodes (R + N), purple to microvilli (MV) and microvilli tips (MT).

D, E   Staticity scores for different surface features (R + N, MV; D) and for segmented IgM-BCR clusters assigned to different surface features (E) in untreated and 15–30 min 100 μM CK-666-treated cells. Violin plot solid lines represent the median and dotted lines represent the quartiles.

F   IgM-BCR intensity enrichment within the segmented clusters at different surface features. Intensity enrichment was measured by dividing the average voxel intensity in the IgM-BCR clusters (μ_{ci}) by the average voxel intensity of the non-clustered ("diffuse") IgM-BCR residing within the surface feature mask (μ_{di}). Data points and the error bars represent mean ± SD.

G   Continuous analysis of IgM-BCR cluster density in 15–30 min 100 μM CK-666-treated cells using geodesic distance maps initiating from distinct surface features (centerline of ridges, nodes and microvilli tips; to compare with untreated in Fig 3F). Data points and the dotted lines represent mean ± SD.

H   Time-course images of EGFP-CaaX and IgM-BCR intensity in an elongating microvillus in an untreated cell (purple, microvilli mask). Scale bar = 1 μm.

Data information: *n* = 7 (30-time frames/cell) for untreated cells from four independent experiments and *n* = 5 (30 to 50-time frames/cell) for CK-666 treated cells from two independent experiments. Two-tailed, unpaired Student *t*-test was used in (D–F). **P* < 0.05, ***P* < 0.01, ****P* < 0.001, *****P* < 0.0001. Comparison in (D) between UT and CK-666 at R + N, *P* = 0.0001; at MV, *P* = 0.0258. Comparison in (E) between UT and CK-666 at R + N, *P* = 0.0001; at MV, *P* = 0.001. Comparison in (F) between UT and CK-666 at SI, *P* = 0.0003.
Source data are available online for this figure.

A Skeletonized R network + MV

B Segmented IgM-BCR clusters

C IgM-BCR clusters at surface features

Sum projection along time axis (37.5 s)

Untreated

CK-666

SI / R+N / MS+MT

D staticity score for skeleton (IOU)

E staticity score for clusters (correlation)

F cluster intensity fold change (μ_{cl}/μ_{dij})

G CK-666 — cluster density (cluster count per µm³) / Geodesic distance

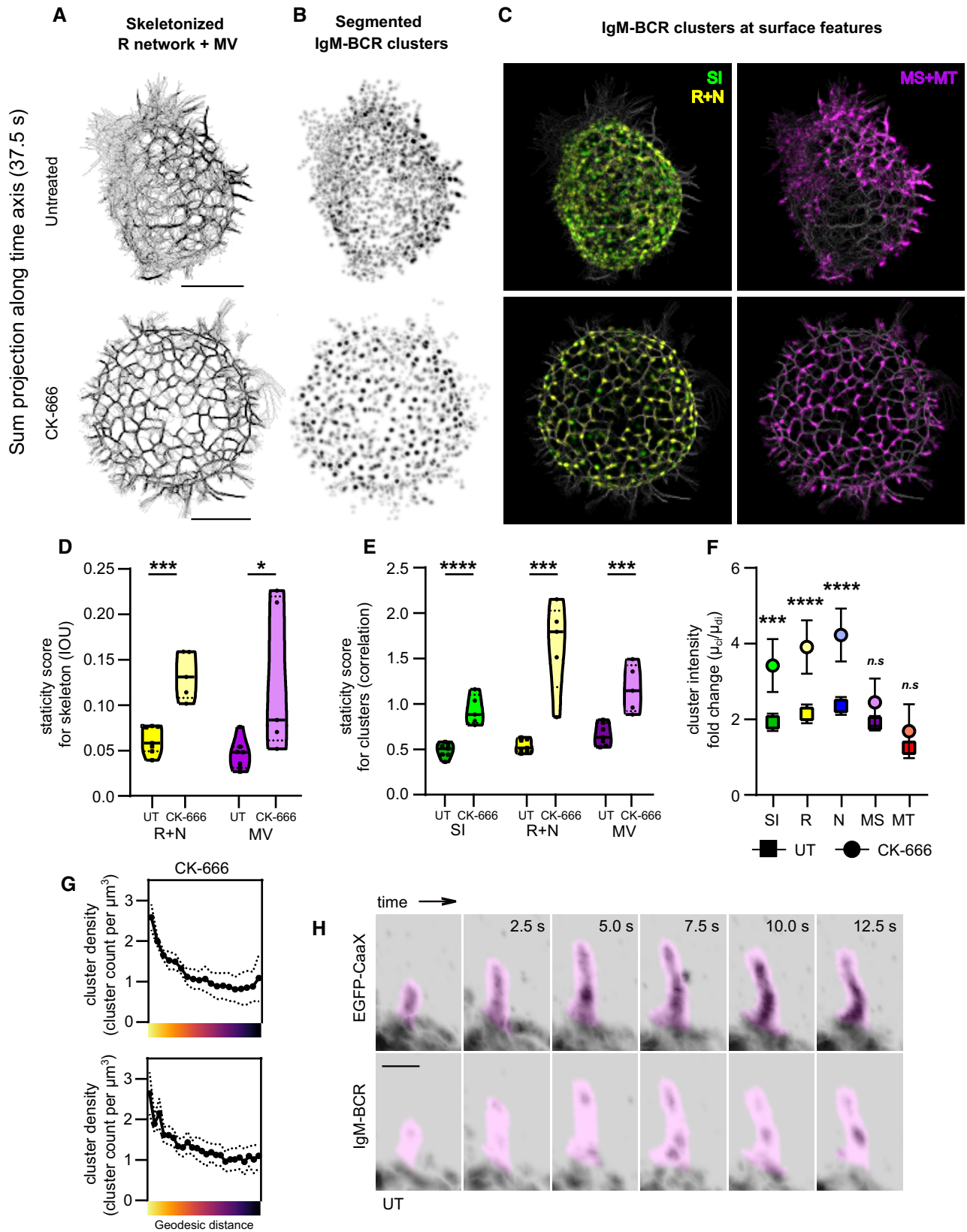**H** time → EGFP-CaaX / IgM-BCR / UT — 2.5 s, 5.0 s, 7.5 s, 10.0 s, 12.5 s

Figure 4.

synapse. Ag-MC became immobilized on the elevated regions, displaying higher staticity scores and bright cluster centroid sum projection images (Fig 6H and I). Depolymerizing the microtubule cytoskeleton for 30 min after LatA incubation (30 min) and prior to antigen stimulation did not alter the immobilization of Ag-MC on the elevated regions (Fig EV4C and Movie EV11). In conclusion, the basic surface patterning governing IgM-BCR cluster localization dynamics and anchoring of IgM-BCR to elevated surfaces are regulated by mechanisms operating upstream of the actin and microtubule cytoskeletons.

Discussion

Analyzing the Ramos B cell surface in 4D, apart from the well-documented lymphocyte microvilli (Majstoravich *et al*, 2004; Orbach & Su, 2020), we observed an elevated, continuous and
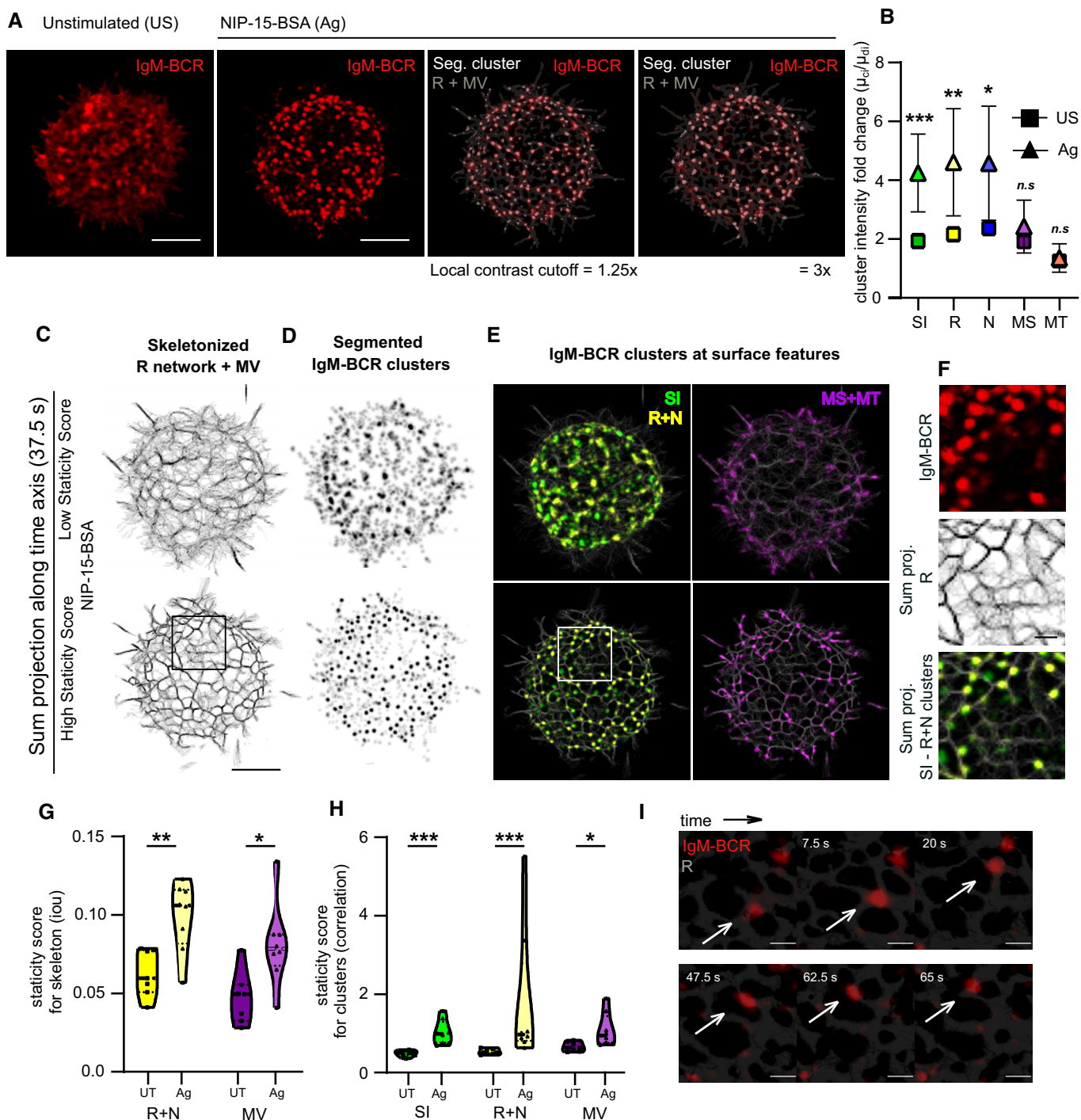

Figure 5.

Figure 5. Antigen-induced micro-clusters (Ag-MC) localize to and move on the ridge network.

A   IgM-BCR cluster distribution upon Ag stimulation. Ramos B cells in the Matrigel were stimulated with 50 ng/ml NIP-15-BSA Ag. Ag-MC on the B cell surface were segmented and overlaid with the ridge network (including microvilli) with a 1.25× and 3.0× local intensity cut-off for cluster detection. Scale bar = 5 μm.
B   IgM-BCR intensity enrichment within the segmented clusters at different surface features for unstimulated (US) and Ag-stimulated cells. Intensity enrichment was measured by dividing the average voxel intensity in the IgM-BCR clusters (μ_{ci}) by the average voxel intensity of the non-clustered ("diffuse") IgM-BCR residing within the different surface feature masks (μ_{di}). Data points and the error bars represent mean ± SD.
C, D   Sum projections of the skeletonized ridge network and microvilli (C) and segmented IgM-BCR clusters (D) in Ag-stimulated cells with a low and high staticity score (duration: 37.5 s). Scale bar = 5 μm.
E   Color coding of the segmented IgM-BCR clusters in (D) according to their assigned surface feature. Green clusters correspond to shallow invaginations (SI), yellow to ridges plus nodes (R + N), purple to microvilli (MV) and microvilli tips (MT).
F   Close-up of the encircled region in (E) displaying IgM-BCR localization, sum projections of the ridge network and segmented clusters. Ridge network lacking Ag-MC are not stabilized. Scale bar = 1 μm.
G, H   Staticity scores for different surface features (R + N, MV; G) and for segmented IgM-BCR clusters assigned to different surface features (H) in unstimulated and Ag-stimulated cells. Violin plot solid lines represent the median and dotted lines represent the quartiles.
I   Time course images of an Ag-MC undergoing displacement on ridges. Scale bar = 1 μm.

Data information: $n = 7$ (30-time frames/cell) for unstimulated cells from four independent experiments and $n = 8$ (10–50-time frames/cell) for Ag-stimulated cells from four independent experiments. Two-tailed, unpaired Student t-test was used in (B), (G), (H), except for R + N of (H), where non-parametric Mann–Whitney U test was used. *$P < 0.05$, **$P < 0.01$, ***$P < 0.001$. Comparison in (B) between US and Ag for SI, $P = 0.0006$; at R, $P = 0.0039$; at N, $P = 0.0107$. Comparison in (G) between US and Ag at R + N, $P = 0.003$; at MV, $P = 0.012$. Comparison in (H) between US and Ag at SI, $P = 0.001$; R + N, $P = 0.0006$; at MV, $P = 0.0299$.
Source data are available online for this figure.

dynamic surface structure that interconnects neighbouring microvilli, which we termed the ridge network. A similar structure, named micro-ridges, has been found on blood-purified lymphocytes by scanning electron microscopy (Fernández-Segura *et al*, 1994). Cumulative surface coverage of mobile microvilli has been proposed as a mechanism in Jurkat T cells to survey opposing membranes for antigens (Cai *et al*, 2017). On Ramos B cells, ridges cover more surface area in a given time span compared with microvilli. IgM-BCR clusters are found to be enriched on both the ridges and microvilli. The elongation of microvilli is associated with the recruitment of IgM-BCR clusters moving towards microvilli tips. The inhibition of the Arp2/3 complex blocks ridge movements, halts microvillus elongation and leads to arrested, larger IgM-BCR clusters, most notably at nodes (which include microvilli roots). We propose that Arp2/3 complex activity is necessary for the coordinated localization of IgM-BCR on microvilli, and ridges function in antigen surveillance

and as receptor reservoir. We think that the amount of IgM-BCR carried to the microvilli could be subjected to regulation by environmental signals. Movement of IgM-BCR clusters from microvilli roots towards the tips could further serve to reduce the threshold for BCR activation, as the transmembrane phosphatase CD45 that negatively regulates BCR activation has been found to be excluded from microvilli tips (Jung *et al*, 2021).

The spherical morphology that we studied here is likely to occur in circulating B cells. Within tissues or during a germinal center reaction, however, lymphocytes display a migratory phenotype, which is subjected to frequent reorganization of polarity. We speculate that the convergence of receptor and ridge network dynamics (via the Arp2/3 complex) may be an important factor in regulating receptor redistribution during rapid shape changes. Moreover, a system organized as a surface-spanning network may have an advantage in rapidly responding to environmental cues that may arise from any direction.

Figure 6. LatA-induced surface elevations anchor IgM-BCR.

A   Phalloidin-Alexa555 staining of fixed and permeabilized Ramos B cells expressing EGFP-CaaX and IgM-BCR with or without 2 μM LatA treatment for 30 min. Scale bar = 5 μm.
B   Topographical features of the Ramos B cell surface in a cell treated with 2 μM LatA for 15–30 min. LatA-treated cells display disorganized and polarized elevations. The cell is morphologically separated into smooth (green) and elevated (yellow) regions. Scale bar = 5 μm.
C   Time frames from a LatA-treated cell in which stable elevations undergo merging. Scale bar = 1 μm.
D   Surface-masked EGFP-CaaX and IgM-BCR signal and overlay of segmented elevations (yellow) with the surface-masked IgM-BCR signal in cells treated with LatA and LatA+Ag (50 ng/ml NIP-15-BSA). Scale bars = 5 μm.
E   Time frames from a LatA+Ag cell showing directed movement of Ag-MC towards the elevations (yellow). Each Ag-MC shown with a different colored arrow. Scale bar = 1 μm.
F   IgM-BCR intensity enrichment within all the segmented clusters in LatA and Lat + Ag cells.
G   Cluster density at surface features. Quantification of the IgM-BCR cluster density in terms of cluster count per surface feature volume for all segmented IgM-BCR clusters (left panel, local contrast cutoff = 1×) and for Ag-MC (right panel, local contrast cutoff = 3×).
H   Staticity scores for segmented IgM-BCR clusters on smooth and elevated regions in LatA and LatA+Ag cells.
I   Surface-masked EGFP-CaaX and IgM-BCR signal for a LatA and LatA+Ag cell and the sum projections of their segmented IgM-BCR clusters (duration: 37.5 s). IgM-BCR clusters are color-coded (green and yellow) according to their assigned surface region. Scale bar = 5 μm.

Data information: $n = 6$ (50-time frames/cell) for LatA cells from three independent experiments and $n = 7$ (50 time-frames/cell) for LatA+Ag cells from two independent experiments. Violin plot solid lines represent the median and dotted lines represent the quartiles in (F) and (H). Two-tailed, paired Student t-test was used in (G) and two-tailed, unpaired Student t-test was used in (F), (H). *$P < 0.05$. Comparison in (F) between LatA and LatA+Ag, $P = 0.0467$. Comparison in (G) between smooth and elevated in LatA+Ag for 1× cut-off, $P = 0.0260$; for 3× cut-off, $P = 0.0124$. Comparison in (H) between smooth and elevated in LatA+Ag, $P = 0.0143$.
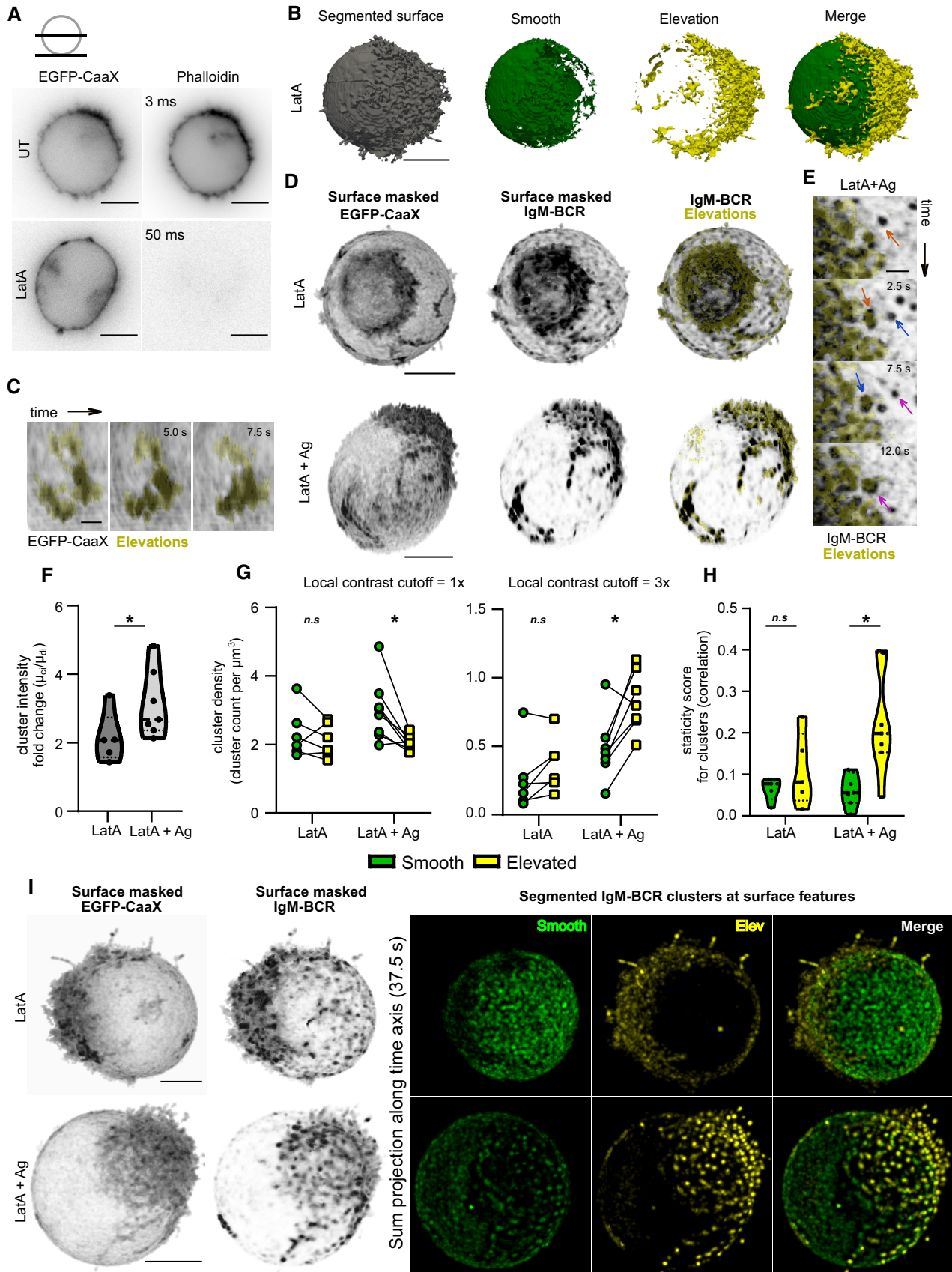Source data are available online for this figure.

Figure 6.

When the actin cytoskeleton is depolymerized, microvilli and ridges mostly retract but a large polarized protrusion with additional disorganized elevations forms on the cell surface. These LatA-induced structures may be the result of the static accumulation of curvature-inducing Bin/Amphiphysin/RVS (BAR) domain-containing proteins (BAR proteins). BAR domains are known to bind and stabilize phosphoinositides (Zhao *et al*, 2013; Suetsugu *et al*, 2014), oligomerize into higher-order patterns (Becalska *et al*, 2013; Simunovic *et al*, 2017), and bend membranes to form dynamic protrusive structures in cooperation with Rho GTPases and Arp2/3 complex-mediated actin polymerization (Suetsugu & Gautreau, 2012; McDonald & Gould, 2016). Actin polymerization seems to provide feedback for their dynamic localization (Wu *et al*, 2018) and the absence of the feedback may result in static membrane bending by some BAR proteins (Becalska *et al*, 2013; Saarikangas *et al*, 2015). In our experiments, LatA did not induce the formation of the static protrusive structure when the microtubule cytoskeleton was depolymerized priorly, an observation in line with Obino *et al* (2016). Microtubule-mediated polarity cues for protrusion formation could involve regulating the phosphoinositide content of the plasma membrane (Golub & Caroni, 2005; Sugiyama *et al*, 2015), asymmetrically activating Rho signaling (Pineau *et al*, 2022) or providing direct interaction with membrane-bending factors (Kelley *et al*, 2015). We think that, once these factors, likely to belong to the BAR protein superfamily, stably bind and bend membranes in the absence of actin cytoskeleton, subsequent microtubule depolymerization is no longer effective.

Our LatA experiments have shown that neither the actin cytoskeleton nor the topographical features are responsible for the clustering of IgM-BCR. However, these factors are involved in the coordinated movement of the receptor clusters on the plasma membrane. In cells devoid of the actin cytoskeleton, on the smoothened regions of the plasma membrane, IgM-BCR clusters are in rapid motion. This observation is in line with TIRF microscopy experiments, where IgM-BCR on the ventral side of LatA-treated B cells become more mobile (Treanor *et al*, 2010; Mattila *et al*, 2013, 2016; Tolar, 2017; Rey-Suarez *et al*, 2020). However, IgM-BCR clusters look trapped in the LatA-induced elevations. We suspect that these regions accumulate a mislocalized scaffold for IgM-BCR, that connects IgM-BCR to outward curvature, which under normal conditions, would couple the receptor to ridge dynamics. The directed motion of Ag-MC on smooth regions towards the LatA-induced protrusions could possibly involve microtubules and dynein (Schnyder *et al*, 2011).

Interestingly, the 3D trajectory of IgM-BCR clusters on smooth regions of LatA-treated cells still seems to form a network of polygonal patterns. Molecules such as phosphoinositides or Rho GTPases display dynamic molecular patterns at the cell cortex as a result of positive and negative feedback loops acting on them (Koch & Meinhardt, 1994; Bement *et al*, 2015; Xiong *et al*, 2016; Michaud *et al*, 2022). It is conceivable that such molecular patterns may form the basis of the network-forming ridges by recruiting curvature-inducing proteins and actin nucleation-promoting factors (Miki *et al*, 2000; Ho *et al*, 2004; Fricke *et al*, 2009; de Kreuk & Hordijk, 2012; Suetsugu & Gautreau, 2012; Becalska *et al*, 2013; Saeng-sawang *et al*, 2013; Aspenström, 2014; Suetsugu *et al*, 2014; Simunovic *et al*, 2017; Wu *et al*, 2018). Our results suggest that the actin cytoskeleton is essential for dynamic 3D topography and proper IgM-BCR localization. However, an additional molecular layer with the capacity to form cortical patterns seems to play a role in recruiting IgM-BCR and controlling actin polarization to position the receptor clusters on the elevated surface structures.

We propose that the germinal center-derived Ramos B cell is a good model system to study questions related to microvilli and surface topography, as it expresses many of the microvilli-associated molecules common to lymphocytes (Appendix Table S1; Hao *et al*, 2008). Regulation of lymphocyte surface structures is a fairly unexplored area and many of the molecules discovered in the context of intestinal microvilli and stereocilia are not expressed by lymphocytes (Appendix Table S2). We think that insight into antigen surveillance in connection with the 3D compartmentalization of the B cell surface may open new avenues for better vaccine design.

Materials and Methods

Ramos B cell line culture

Ramos B cells were cultured in RPMI-1640 Medium with Gluta-MAX™ (Art. No. 61870010, ThermoFisher Scientific) supplemented with 10% fetal calf serum (Cat. No. P30-3302, Lot No. P140508, PAN), 10 U/ml penicillin–streptomycin (Ref. 15140-122, Gibco) and 10 mM HEPES (Ref. 15630-056, Gibco). All cell lines were cultured in a 37°C incubator with 5% CO_2.

Cloning

SNAP-IgM-BCR

Geneblocks (IDT) encoding the b1-8 leader sequence and EGFP was amplified with the primer pair CCCTCGTAAAGAATTCATGGGATGG AGCTGTATCATCCTC and GTCGGCGAGCTGACG. Geneblocks encoding the linker with the A(EAAAK)₃A amino acid sequence and the heavy chain variable region specific for the hapten NIP were amplified with the primers GCGTGCAGCTCGCCGACCACTACCAG CAGAACACCCC and TGAGGAGACTGT GAGAGTGGTGC. Plasmid encoding the mouse μ heavy chain was amplified with the primers TCTCACAGTCTCCTCAGAGAGTCAGTC and GAGGTGGTCTGGAT CCTCATTTCACCTT GAACAGGGTGAC. The three fragments were fused using the in-fusion HD enzyme premix (Cat. No. ST0345, Takara) into a pRetroX-TetOne-Puro (Cat. No. 634309, Takara) backbone using the EcoRI-HF (Cat. No. R3101, NEB) and BamHI-HF (Cat. No. R3136, NEB) restriction sites. Next, the region encoding the three fused sequences was amplified with GAGGTTAACGAATT CATGGGATGGAGCTGTATCATC and CCAGCCTGCTTCAGCAGGCT GAAGTTAGTAGCTCCGCTTCCTGATTTCACCTTGAACAGGGTGACG. The mouse λ light chain with specificity for NIP was amplified with the primers TGCTGAAGCAGGCTGGAGACGTGGAGGAGAACCCTG GACCTATGGCCTGGATTTCACTTATACTCTCTC and TGGCTGCAG GTCGACCTAGGAACAGTCAGCACGGGA. The two fragments were fused using the in-fusion enzyme into a pM retroviral vector cut with EcoRI-HF and SalI-HF (Cat. No. R3138, NEB) restriction enzymes. The primers contained the coding sequence for the P2A cleavage site in between the μ heavy and λ light chains. Next, myc-tag was inserted at the C-terminus of heavy chain with the primer pair CAGAAACTGATCTCTGAGTTCGAGCTGAACGGAAGCGGAGCT ACTAAC and CTCCCCAGAGGCAGCTCCTCCGCCTGATTTCACCTT GAACAGG using the Q5 site-directed mutagenesis kit (Cat. No.

E0554, NEB). Finally, b1-8 leader-EGFP was switched to a b1-8 leader-SNAP-tag by amplifying the SNAP-tag sequence with GAGGTTAACGAATTCATGGGATGGAGCTGTATCATCCTCTTCTTG GTAGCAACAGCTACAGGTGTCCACTCCATGGACAAAGACTGCGAA ATGAAGCG and TCTGCTGGCGGCCGACCCAGCCCAGGCTT and cloning into the plasmid with the in-fusion enzyme using the EcoRI-HF and NotI-HF (Cat. No. R3189, NEB) restriction sites before and after the b1-8 leader-EGFP sequence.

EGFP-CaaX

EGFP sequence was amplified with the primers CGAGGTTAACGA ATTCCATGGTGAGCAAGGGC and ATTTTATCGATAAGCTTCTACA TAATTACACACTTTGTCTTTGACTTCTTTTTTCTTCTTTTTA. The amplified fragment was cloned into pM retroviral vector cut with EcoRI-HF and SalI-HF restriction enzymes using the in-fusion enzyme.

SNAP-CD40

cDNA encoding CD40 was amplified from the cDNA pool of Ramos B cells with the primer pair CGAGGTTAACGAATTCATGGTTCG TCTGCCTCTGC and GCCGCTTCCGCCTCC CTGTCTCTCCTGC. EGFP was amplified with the primers GGAGGCGGAAGCGGCGT GAGCAAGGGCGAGG and ATTTTATCGATAAGCTTTCACTTGTAC AGCTCGTCCATGCC. The two fragments were inserted into a pM retroviral vector cut with EcoRI-HF and HindIII-HF with the in-fusion enzyme. Next, CD40 sequence was amplified with GGAGGC GGAAGCGGCGAACCACCCACTGCATGC and TTTTATCGATAAGCT TTCACTGTCTCTCCTGCACTGAGATG. SNAP-tag sequence with an N-terminal b1-8 leader sequence was amplified with CGAGGTTAAC GAATTCATGGGATGGA and GCCGCTTCCGCCTCCACCCAGCCCA GGCTG. The two fragments were cloned into a pM retroviral vector cut with EcoRI-HF and HindIII-HF using the in-fusion enzyme.

Generation of the Ramos B cell lines with retrovirus

H/L chain locus of Ramos B cells was silenced using the CRISPR-Cas9 technology. For a detailed protocol, refer to (He et al, 2018). The retroviral plasmids encoding SNAP-IgM-BCR, EGFP-CaaX and SNAP-CD40 were transfected (1,000 ng) along with the pKat plasmid encoding the viral coat protein (500 ng) into the Platinum-E ecotropic retroviral packaging cell line (Cat. No. RV-101, Cell Biolabs) using the transfection reagent PolyJet (Cat. No. SL100688, SignaGen) in a 6-well plate format. Platinum-E cells were maintained in the RPMI cell culture medium. The virus containing supernatant was collected for each plasmid after 48 h. 500,000 H/L-KO Ramos B cells were first transduced with the EGFP-CaaX retrovirus supernatant in a 1:1 ratio for 4 h in a 37°C incubator with 5% CO_2. Cells were resuspended in fresh culture medium and incubated for another 7 days before sorting for the EGFP signal with a BioRad cell sorter. Sorted cells were transduced another round either with retrovirus encoding SNAP-IgM-BCR or SNAP-CD40 using the same protocol. Cells were stained with SNAP-Surface® 549 (DY549P1; Cat. No. S9112, New England Biolabs) for 15 min in a 37°C incubator with 5% CO_2 and sorted for the fluorescent signal.

Calcium flux measurements upon antigenic stimulation

1 million cells per ml were loaded with 1 μM Indo-1 (Cat. No. I1223, Invitrogen) in 0.1% pluronic-containing cell culture medium for 30 min at a 37°C incubator with 5% CO_2. Loaded cells were washed in cell culture medium three times and rested in the incubator for 30 min. All calcium measurements with one batch of loading were completed within the 45 min following the 30 min resting period. Ratiometric measurements for Indo-1 were performed with BD Facs. The collected data points were saved as a .cvs file using the FlowJo export option. Calcium flux graphs were generated in Mathematica with a home-written code. NIP-15-BSA-Biotin (Cat. No. N-1027-5, Biosearch Technologies), goat F(ab')2 anti-mouse IgM, human adsorbed antibody (Cat. No. 1022-01, polyclonal, Southern Biotech), goat anti-human IgM antibody (Cat. No. 2020-01, polyclonal, Southern Biotech), goat anti-mouse lambda antibody (Cat. No. 1060-01, polyclonal, Southern Biotech) were used to stimulate the cells.

Actin cytoskeleton staining of Ramos B cells

1 million cells were washed in PBS, incubated with the indicated drugs for the indicated times at a 37°C incubator and fixed with 4% PFA for 15 min at RT. Fixed cells were washed three times in PBS, permeabilized with 0.1% Triton-X in PBS for 3 min, blocked in 1% BSA-PBS for 30 min and stained with 0.2 μM Phalloidin-Alexa Fluor 555 (Invitrogen, Cat. No. A34055) in 1% BSA-PBS for 1 h.

Sample preparation for LLSM and imaging

Lattice light-sheet microscopy was performed on a home-built clone of the original design by the Eric Betzig group (Chen et al, 2014). Before imaging, 2 ml of a Ramos B cell suspension was centrifuged for 2 min at 700 g. Afterwards, the supernatant was resuspended in 200 μl fresh cell culture medium together with 1 μM SNAP-Surface® 549. After 15 min of incubation, the cell suspension was washed four times with 2 ml PBS, pH 7.4 at 37°C. In the next step, the cell pellet was resuspended in approximately 20 μl PBS, pH 7.4 and mixed with phenol-red free Corning® Matrigel® Matrix (Product No. 356237, Corning) in a ratio of 1:1. 2 μl of this mix was dropped on a freshly plasma cleaned 5 mm round glass coverslips (Art. No. 11888372, ThermoFisher Scientific). Coverslips were then transferred to a small humidified chamber and incubated at 37°C until gel formation was complete. Then, the coverslip was mounted in a custom-built sample holder that was attached on top of a sample piezo. This ensures that the sample is inserted at the correct position between the excitation and detection objectives inside the sample bath containing PBS, pH 7.4 at 37°C. For the inhibition of the Arp2/3 complex, CK-666 (Cat. No. 3950, Tocris) was added at a concentration of 100 μM to the sample bath. For the destabilization of the whole actin cytoskeleton, 2 μM Latrunculin A (Cat. No. 3973, Tocris) was added to the media bath. In both cases, cells were imaged for up to 1 h. For the depolymerization of the microtubule cytoskeleton, 20 μM nocodazole was added to the sample bath for up to 30 min (Cat. No. 1228, Tocris). For the stimulation of cells via IgM-BCR, 50 ng/ml NIP-15-BSA-Biotin was added to the media bath and images were collected after a short incubation of about 5 min and proceeded for about 30 min. To test the antigen stimulation of cells in CK-666-, Latrunculin A- or nocodazole-treated cells, cells were first incubated for 30 min inside the microscopy chamber with the respective substance before the addition of 50 ng/ml NIP-15-BSA. Imaging was then performed after 5 min and proceeded until 30 min. For image acquisition, a dual-channel image stack was

acquired in sample scan mode by scanning the sample through a fixed light sheet with a step size of 500 nm which is equivalent to a ~ 270 nm slicing with respect to the z-axis considering the sample scan angle of 32.8°. A dithered square lattice pattern generated by multiple Bessel beams using an inner and outer numerical aperture of the excitation objective of 0.48 and 0.55, respectively, was used during the experiments. Channels were sequentially excited using a 488-nm laser (2RU-VFL-P-300-488-B1R; MPB Communications Inc., Pointe-Claire, Canada) for EGFP and a 561 nm laser (2RU-VFL-P-2000-561-B1R; MPB Communications Inc.) for SNAP-Surface® 549. Fluorescence was collected by a water dipping objective (CFI Apo LWD 25XW, NA 1.1, Nikon) and imaged on a sCMOS camera (ORCA-Fusion, Hamamatsu, Japan) with a final pixel size of 103.5 nm. Acquisition was performed at 100 frames per second with an exposure time of 8 ms for each channel.

LLSM data processing

Lattice light-sheet raw data were further processed by using an open-source LLSM post-processing utility called LLSpy (https://github.com/tlambert03/LLSpy) for deskewing, deconvolution, channel registration and transformation. Deconvolution was performed by using experimental point spread functions recorded from 100 nm sized FluoSpheres™ (Art. No. F8801 and F8803, ThermoFisher Scientific) and is based on the Richardson–Lucy algorithm using 10 iterations. For channel registration and alignment, 200 nm sized fluorescent TetraSpeck™ microspheres (Art. No. T7280, ThermoFisher Scientific) were imaged with the same step size of 500 nm as used for cellular imaging. Alignment was done with a 2-step transformation method that deploys an affine transformation in xy and a rigid transformation in z.

Image analysis

Section 1: Segmentation of plasma membrane features

Binary masks for different topographical features of B-cell surface were created by using the following protocol:

1 Creation of a binary mask for the entire plasma membrane surface using the EGFP-CaaX signal.
2 Creation of a binary mask for the inner space of the cell corresponding to the cytoplasm (named "dome" throughout the text).
3 Refinement of the plasma membrane mask from step 1 using the dome from step 2.
4 Extraction of a surface mesh and calculation of the shape index to examine topography.
5 Creation of a binary mask for the ridge network using the EGFP-CaaX signal.
6 Partitioning of the plasma membrane topography into multiple morphological features using the binary masks from step 1, 2, 3 and 5.

Step 1: Binary segmentation of the plasma membrane surface

To perform the binarization of the EGFP-CaaX signal, a 3D segmentation model was trained using the network architecture DynUNet, which is implemented in Project MONAI (https://github.com/Project-MONAI/MONAI/tree/0.8.1). DynUNet itself is modified from nnU-Net developed by Isensee et al (2021). To train this model, we first generated the ground truth dataset by using a semi-automatic segmentation approach. This approach consists of (i) training an unsupervised binary voxel classification model that uses k-means clustering (using scikit-learn 1.0.1) on a multivariate feature space (created using SciPy version 1.7.1), and (ii) manual correction of images segmented by this model and validation of the binary masks by three domain experts. The ground truth dataset was generated from 6 × 3D images, each extracted from a different LLSM time series. The feature extraction for the training of the voxel classifier includes multiscale filtering of the image with a series of filters (filter names and filter parameters provided in Table 1). Manual correction of the preliminary binary masks produced by the voxel classifier was performed using the Napari package version 0.4.12 (Sofroniew et al, 2021) as GUI. Prior to DynUNet model training, the following data augmentations were performed: cropping, contrast adjustments, Gaussian noise injections, Gaussian smoothing, Gibbs noise injections and rotations. The augmentations were performed by using the "transforms" module of the MONAI package. The DynUNet model was then trained based on the parameters and specifications provided in Table 2. The trained model was used to segment each volume in the volumetric time-course data. The output from this segmentation was refined by removing binary objects smaller than 30 voxels.

Step 2: Extraction of the dome

A semi-automatic, robust, watershed-based protocol was developed and applied to extract the dome of the cell directly from the EGFP-CaaX signal. The protocol is based on the automatic selection of two seeds for the interior and exterior of the cell. The algorithm is outlined as follows:

I Binarize the raw image with a low threshold to obtain a rough binary surface object.
II If the surface object contains gaps, use mathematical morphology to close them. Then fill the interior space of the object via binary filling.
III Use binary opening to eliminate any protrusive structures from the filled surface. This leads to a rough dome-like structure. Extract the surface layer of this dome using either mathematical morphology or specifying a level of its distance transform.
IV Compute a distance transform using the surface layer from step III as the zero level.
V Select a distance threshold to specify internal and external seeds from the distance map. For example, a distance threshold of 3 μm will specify an internal patch 3 μm inwards from the

Table 1. Specifications of the filters used in the voxel-wise feature extraction.

Filter Type	Parameter(s)	Value(s)
Minimum	Window (Square Box) Dimension	3 voxels
Gaussian	Sigmas	1, 1.5
LoG	Sigmas	0.8, 0.82, 0.84, 0.9, 0.93, 0.96, 1.0, 1.5
DoG	Sigma1 and Sigma 2	5 and 7
Gray Closing	Window (Sphere) Diameter	5 voxels
White Top-hat	Window (Sphere) Diameter	3 voxels

surface and an external shell enclosing the cell from 3 μm outwards from the surface. Label the internal and external seeds.

VI Generate an input image for the watershed algorithm by calculating a weighted mean of the raw image and the distance map from step IV. The weights can be specified by the user.

VII Perform the watershed segmentation on the input image using internal and external labels as markers. The dome is the component corresponding to the internal label in the output.

Step 3: Refinement of the plasma membrane mask

The plasma membrane mask from (section-1/step-1) usually contains small gaps at the cell surface, which may interfere with the downstream analysis. To close these gaps, we merged the output from (section-1/step-1) and the surface layer of the dome from (section-1/step-2). We subtracted the entire dome object except for its surface layer, from the plasma membrane mask, to ensure that the downstream analysis is confined to the cell surface and the microvilli, and that any other components within the cytoplasm are excluded from the analysis.

Step 4: Calculation of the shape index

The dome from (section-1/step-2) and the plasma membrane mask from (section-1/step-3) was merged via Boolean union operation, leading to an in-filled cell mask. Then a triangular surface mesh was calculated from this cell mask using the PyVista module (Sullivan &

Table 2. Specifications of the segmentation model. Any specifications not disclosed in this table are equal to the defaults implemented in the MONAI version 0.7.0 (Version 0.7.0 10.5281/zenodo.5525502).

Model architecture	DynUNet (https://docs.monai.io/en/stable/networks.html#dynamic-unet-block)
Number of spatial dimensions	3
Number of input channels	1
Number of output channels	2
Convolution kernel size	(1, 3, 3, 3)
Convolution strides (= upsample kernel size)	(1, 2, 2, 2)
Dropout	None
Normalization	Instance normalization
Activation layer	Leakyrelu
deep supervision	False
Residual connections	True
Loss function	DiceCELoss (https://docs.monai.io/en/stable/losses.html#diceceloss)
to_onehot_y	True
softmax	True
squared_pred	True
Batch	True
Optimiser	Novograd (https://docs.monai.io/en/stable/optimizers.html#novograd)
Learning rate	1e-2

Kaszynski, 2019, https://github.com/pyvista) version 0.32.1. Subsequently, principal curvatures of the surface topography were calculated from this mesh using the igl library (https://libigl.github.io/) python bindings version 2.2.1. Finally, the shape index was calculated by plugging the principal curvatures in the following equation (according to the study by Koenderink & van Doorn (1992)):

$$S = \frac{2}{\pi}\arctan\frac{K2 + K1}{K2 - K1}\,(K1 \geq K2),$$

where *K1* and *K2* are the larger and smaller principal curvatures, respectively.

Step 5: Extraction of the ridge mask and the skeleton

Hessian-based approaches are frequently used for the detection and segmentation of curvilinear objects (Zhao et al, 2019). Here the following pipeline was used for the extraction of the ridges:

I Apply a Hessian-based vesselness filter (Sato et al, 1998; implemented in ITK version 5.2.1) to the intensity image.

II Rescale the values of the Hessian response image between 0 and 1.

III Binarize the rescaled Hessian response image using a combination of local and global thresholding, as described below:

$$c = max - min$$
$$L = 0.2 \times (min + max)$$
$$t = \begin{cases} g, & I(i) < c(i) \\ L(i), & I(i) \geq c(i) \end{cases}$$
$$T = \begin{cases} 0, & I(i) < t(i) \\ 1, & I(i) \geq t(i) \end{cases}$$

where *I* is the image array and *i* is the voxel index; *max* and *min* are the local maxima and local minima transforms of the image, respectively, calculated with a spherical local window having a diameter of 7 voxels; *g* is a user-specified global threshold. Here we used multi-otsu thresholding (Liao et al, 2001), implemented in scikit-image (version 0.18.3) to calculate four thresholds and assigned the lowest threshold to *g*; *t* is the local threshold; *T* is the final thresholded image.

IV Subject the thresholded image to one round of closing operation with a spherical structuring element in a window of (3, 3, 3). The output from this process is the ridge mask.

V Subject the binary ridge mask from step IV recursively to steps I to IV. This yields a thinned form of the ridge mask.

VI Apply 3D morphological skeletonization (Lee et al, 1994), implemented in scikit-image (version 0.18.3) to the thinned ridge mask from step V. The output from this process is the 1-voxel thick ridge skeleton.

Step 6: Partitioning of the plasma membrane mask into its topographical features

Step 6A: Partitioning of the cells that are not treated with LatA By using the outputs from (section-1/steps-2, 3 and 5), the topographical features of the plasma membrane mask were identified. This process is further divided into multiple steps as described below.

Step 6A/a: Separating the protrusive structures (microvilli) from the cell body:

The pipeline, which is based on binary mathematical morphology, is outlined below:

I   Calculate the union of the dome from section-1/step-2 and the plasma membrane mask from section-1/step-3 to obtain an "in-filled" cell mask.
II Apply a binary opening filter to the output from step 1using a box-shaped structuring element. We used a structuring element of voxel size (3, 5, 5).
III Apply a binary opening filter to the output from step II using an ellipsoidal structuring element. We used a structuring element of voxel size (5, 7, 7).
IV Calculate the intersection of the output from step III and the plasma membrane mask. This process yields the cell body mask.
V   Subtract the cell body mask from the plasma membrane mask. This process yields the microvilli mask.

Step 6A/b: Extraction and annotation of the ridge network:

A custom algorithm was applied to the ridge skeleton from section-1/step-5 to detect and label microvilli tips and ridge junctions. In the first step of the algorithm, the skeleton vertices are annotated based on the local sum in a (3, 3, 3) neighbourhood of each vertex as described in the following:

$$V_{neigh}(i,j,k) = \sum_{(m,n,p) \in S_{ijk}} V(m,n,p),$$

where V is the skeleton image; V_{neigh} is the local sum evaluated over the skeleton; m, n and p are the coordinates in the local window of (3, 3, 3) around the point (i, j, k); i, j and k are the global coordinates.

The annotation is then performed as described below:

$$L(i,j,k) = \begin{cases} 2, & V_{neigh}(i,j,k) = 1 \rightarrow Edge\ label \\ 1, & V_{neigh}(i,j,k) = 2 \rightarrow Tip label \\ 3, & V_{neigh}(i,j,k) > 3 \rightarrow Node\ label \end{cases}$$

where L is the label image.

In the second step of the algorithm, a correction function to the label image was applied, which recognizes very short edges (< 200 nm) and replaces them with a node label. We then used our feature masks from section-1/step-6A/a to confine the annotations. Namely, the cell body mask was used to confine the nodes and edges to the cell body and the microvilli mask was to confine the tips to the microvilli.

Step 6A/c: Construction of the feature images:

Three geodesic distance maps per cell were computed based on the labeled network image from section-1/step-6A/b using the fast marching method (implemented in scikit-fmm version 2021.10.29). The first geodesic map (gdmap_skeleton) was computed by assuming the intersection of the skeleton and the cell body mask as the zero level set and the cell body mask as the speed image. The second geodesic map (gdmap_tips) was computed by assuming the tips as the zero level set and the microvilli mask as the speed image. Finally, the third geodesic map (gdmap_nodes) was computed by assuming the nodes as the zero level set and the cell body mask as the speed image.

After computing the geodesic distance maps, the final topographical features were computed as follows:

• Microvilli tips mask was obtained by applying a threshold of 2.1 to the gdmap_tips.
• Microvilli shaft mask was obtained by subtracting the microvilli tips mask from the microvilli mask.
• Cell body node mask was obtained by applying a threshold of 1.5 to the gdmap_nodes.
• Cell body ridge mask was obtained by applying a threshold of 2.7 to the gdmap_skeleton and then subtracting the cell body node mask from the resulting binary mask.
• Cell body shallow invaginations mask was obtained by subtracting the union of the cell body ridge mask and the cell body node mask from the cell body mask

Step 6B: Partitioning of the LatA-treated cells Cells that were treated with LatA displayed a generally smooth surface with occasional, bulky stacks of the membrane. As these cells did not show an organized ridge network, they were not suitable for partitioning using the approach described in section 1/step 6A. The LatA-treated cells showed a surface topography that contained short stretches of curvilinear elevations as well as disorganized blob-like chunks of the membrane with varying sizes. To detect both types of structures, two detection filters for each raw image were separately applied, one for curvilinear structures (Jerman *et al*, 2016b) and one for blob-shaped structures (Jerman *et al*, 2016a). To detect structures of different sizes, each filter was applied at multiple scales, using sigma values of 1 and 2 for the curvilinearity filter and sigma values of 1, 2 and 3 for the blob filter. Then each response image was segmented using a global threshold, which was generally chosen to be the Otsu threshold (Otsu, 1979) but varied when necessary. When the binary masks were obtained for both curvilinear and blob-shaped structures, these were combined using a Boolean union filter to obtain a preliminary "elevation" mask. Finally, a watershed segmentation was applied to delineate the elevation mask. For this watershed step, we selected the preliminary elevation mask as marker 1, the dome from section 1/step 2 as marker 2 and the negative of the Euclidean distance transform of the cell surface mask from section 1/step 3 as the main input image. As a result of the Watershed segmentation, the label corresponding to marker 1 was designated as the elevation mask and the label corresponding to marker 2 was designated as the cell body mask.

Section 2: Segmentation of IgM clusters

It was asserted that a voxel patch must meet the following criteria to be assumed as a cluster.

Cluster criteria:

1 The patch has intensities that are significantly higher than its neighbourhood.
2 The patch has a size (voxel count) below a size threshold.

To extract patches that meet criterion 1, a two-step algorithm was developed, which uses a custom local thresholding function with hyperparameters adaptive to different images. The two steps are outlined as follows:

Step 1: Extract a "blob" mask

A blob mask is a binary image calculated from local curvature cues that are derived from the raw image. The local curvature cues are the eigenvalues of the Hessian matrix $H(f)$:

$$H(f) = \begin{matrix} h_{11} & h_{12} & h_{13} \\ h_{21} & h_{22} & h_{23} \\ h_{31} & h_{32} & h_{33} \end{matrix} = \begin{matrix} \frac{\partial^2 f}{\partial x_1^2} & \frac{\partial^2 f}{\partial x_1 \partial x_2} & \frac{\partial^2 f}{\partial x_1 \partial x_3} \\ \frac{\partial^2 f}{\partial x_2 \partial x_1} & \frac{\partial^2 f}{\partial x_2^2} & \frac{\partial^2 f}{\partial x_2 x_3} \\ \frac{\partial^2 f}{\partial x_3 x_1} & \frac{\partial^2 f}{\partial x_3 \partial x_2} & \frac{\partial^2 f}{\partial x_3^2} \end{matrix}$$

where f is convolution of the image I with a Gaussian kernel (we used a sigma value of 1).

The eigenvalues λ_1, λ_2 and λ_3 were calculated from the $H(f)$. Subsequently, the blob mask B was calculated as below:

$$B(\lambda_i) = \begin{cases} 1, & \lambda_i < Tk \\ 0, & Otherwise, \end{cases}$$
$$with\ \lambda_i = \{\lambda_1, \lambda_2, \lambda_3\}$$

where T is the Otsu threshold of the negative values of λ_i and k is a user-specified value (we selected the value of 0.01 for an over-segmentation). Finally, the blob mask B was calculated as the intersection of the components:

$$B = B(\lambda_1) \cap B(\lambda_2) \cap B(\lambda_3)$$

The blob mask calculated in this manner contains nearly all possible voxel patches that can be extracted from a grayscale image I. These patches are treated as "candidates" to be clusters.

Step 2: Find optimal local signal thresholding hyperparameters

A local thresholding function based on a modification of the Niblack threshold method (Niblack, 1985) was used in that the binarization via local thresholding is restricted to the high-contrast regions in the image as expressed below:

$$T = I_{mean} + kI_{std}$$
$$C = I_{max} - I_{min}$$
$$f(k,l) = \begin{cases} 1, & I > T, C > l \\ 0, & Otherwise \end{cases}$$

where I_{mean}, I_{std}, I_{max}, I_{min} are arrays with local means, standard deviations, maxima and minima, respectively, calculated using a square-box local neighbourhood with a window size of 5 voxels; T is the Niblack threshold and C is the local contrast.

The segmentation function f is then dependent on the hyperparameters k and l, which must be optimized for segmenting the clusters of a particular image. To this end, we applied a grid search for a series of k and l and chose the binary mask with greatest similarity to the blob mask B from (section 2/step-1). In other words, for a specific image I, we applied:

$$minimise(1 - similarity(B_I, f_I(k,l)))$$

where we used the Tversky method (Tversky, 1977) as the similarity function between the two binary images. This process segments any existing clusters (blob-shaped elements) in the image, however, high-contrast objects that are not actually clusters (e.g., flat or elongated objects) are also binarized. To find the relative volume of the clustered signal compared with that of the non-clustered signal, we applied a size threshold to the output from the cluster segmentation process.

Step 3: Apply a size threshold

The output image from (section-2/step-2) was filtered with a size threshold so that binary objects with a voxel count greater than a user-specified threshold are ruled out from being considered clusters. A size threshold of 75 voxels was selected for this step and the output was designated M_c (cluster mask).

Step 4: Locate centroids and apply feature-based contrast threshold

The centroid of each cluster from (section-2/step-3) was located and labeled and designated C_c (cluster centroids). Subsequently, the ratio of the IgM intensity at each cluster centroid to the mean intensity of the corresponding morphological feature was calculated. The output is a map of feature-based intensity fold increase at cluster centroids. Finally, a threshold was applied to this map so that any centroids with a ratio lower than a given threshold are deleted. Depending on the analysis, this threshold was specified as 1.25 or 3, meaning that each centroid must have an intensity of 1.25-fold (for moderate stringency) or 3 fold (for high stringency) higher than the mean intensity of the corresponding morphological feature.

Analysis

Granularity

Granularity was defined as the ratio of the voxel count of the size-filtered binary objects (clusters, output from section-2/step-3) to the total voxel count of the binary objects yielded by the cluster segmentation protocol (clusters + non-clustered binary objects, output from section-2/step-2).

Feature-based cluster density

Feature-based cluster density is the ratio of the cluster count within a particular morphological feature to the total volume of that feature.

$$d_D = \frac{\sum C \cap D}{v \sum D}$$

where d_D is the cluster density for a particular morphological feature; D is the mask for the morphological feature in question; C is the centroid mask and v is the voxel volume for the image.

Cluster density plotted with geodesic distance

To analyze the cluster density in relation to geodesic distance, the geodesic distance maps from (section-1/step-6A/c) were divided into equal-sized bins so that each bin represents a particular geodesic distance range. Then the cluster density was calculated within each bin as described below:

$$D_H = \begin{cases} 1, & gdmap > value0 \ AND \ gdmap \leq value1 \\ 2, & gdmap > value1 \ AND \ gdmap \leq value2 \\ 3, & gdmap > value2 \ AND \ gdmap \leq value3 \\ 4, & gdmap > value3 \ AND \ gdmap \leq value4 \\ & \cdots \\ i, & gdmap > valuei-1 \ AND \ gdmap \leq valuei \end{cases}$$

$$d(i) = \frac{\sum C \cap D_H(i)}{v \sum D_H(i)}$$

where D_H is the binned image; i is the index to a particular bin (hence represents geodesic distance); $d(i)$ is the density calculated for the particular bin indexed by i.

Global cluster enrichment

Global cluster enrichment is defined as the fold increase of the global mean value of clustered IgM signal over the global mean value of non-clustered IgM signal:

$$MCI = \frac{\sum I \cap M_C}{\sum M_C} \qquad MNCI = \frac{\sum I \cap M_{NC}}{\sum M_{NC}}$$

$$CE = \frac{MCI}{MNCI}$$

where I is the grayscale image; M_C is the cluster mask; M_{NC} is the non-clustered surface mask; MCI is the mean clustered intensity; $MNCI$ is the mean non-clustered intensity; CE is the cluster enrichment.

Cluster enrichment per feature

Cluster enrichment per feature is defined as the fold increase of the mean value of clustered IgM signal within a particular morphological feature over the global mean value of non-clustered IgM signal:

$$MCI_D = \frac{\sum I \cap (M_C \cap D)}{\sum M_C \cap D} \qquad MNCI = \frac{\sum I \cap M_{NC}}{\sum M_{NC}}$$

$$CE_D = \frac{MCI_D}{MNCI}$$

where D is the binary mask for a specific morphological feature; MCI_D is the mean clustered intensity within feature; CE_D is the cluster enrichment for feature D.

Proportion of the clustered intensities

To calculate the proportion of clustered signal, the summed value within the cluster mask was divided into the summed value within the entire surface mask (clustered + non-clustered):

$$PCI = \frac{\sum I \cap M_C}{\sum I \cap (M_{NC} \cup M_C)}$$

where PCI is the proportion of the clustered intensities.

Calculation of staticity for cluster centroids

To create a staticity map, a 4D segmented image (the volumetric time-course) for the cluster centroids was correlated with a 4D Gaussian kernel. This correlation operation yields a stronger response with cluster centroids that remain within a close neighbourhood compared with centroids that undergo large displacements. In other words, voxels corresponding to relatively immobile centroids have high values on the map, whereas voxels corresponding to highly dynamic centroids have low values. Once we had the staticity map, we calculated the staticity as the proportion of voxels higher than a user-defined threshold. Therefore:

$$SM = C_c \otimes g$$

$$SM_H = \begin{cases} 1, & SM > T \ and \ D > 0 \\ 0, & otherwise \end{cases}$$

$$SM_L = \begin{cases} 1, & SM \leq T \ and \ D > 0 \\ 0, & otherwise \end{cases}$$

$$S = \frac{\sum SM_H}{\sum SM_L}$$

where C_c is the binary input image for cluster centroids, which is subjected to the staticity analysis; SM is the staticity map; D is the binary feature mask to limit clusters within a specific surface feature; g is the Gaussian kernel with shape (7, 5, 5, 5) voxels and weights (3, 1, 1, 1) in the order of (t, z, y, x); S is the staticity term; T is the user-defined threshold (we used the value 0.15 for all datasets).

The staticity was calculated for the first 15 frames of each time-course image.

Calculation of staticity for surface features

With label images of surface features, staticity was calculated based on the similarity of consecutive time frames. To measure similarity, the intersection over union (IOU) method was used. Highly dynamic surface features undergo large displacements between time frames resulting in low IOU scores, whereas relatively immobile features yield high IOU scores. The staticity is then the mean of the IOU scores calculated for all consecutive pairs along the first 15 frames of each time-course dataset.

Therefore:

$$S = \frac{1}{15} \sum_{t=1}^{15} \frac{D(t-1) \cap D(t)}{D(t-1) \cup D(t)}$$

where S is the staticity term; D is the binary input image for one of the computed surface features, which is subjected to the staticity analysis; t is the time frame.

Statistics and reproducibility

Statistical analyses were performed using GraphPad Prism. Experiments were performed independently, repeated at least twice and similar results were obtained from each cell imaged. Data collection was not performed blindly. Data was only excluded when the image quality did not suffice for image segmentation and analysis. Distribution was assumed as normal for statistical analysis, except for Fig 5H (R + V). For statistical analyses, two-tailed paired or unpaired Student's t-tests or Mann–Whitney U test were performed, as specified in the figure legends. Significance was drawn at $*P < 0.05$. Significance was defined as $****P < 0.0001$, $***P < 0.001$, $**P < 0.01$.

Data availability

Lattice light-sheet volumetric time-series image data used for this publication have been submitted to Bioimage Archive in a channel registered, deskewed and deconvolved form with the accession number S-BIAD573 (https://www.ebi.ac.uk/biostudies/studies/S-BIAD573?key=6ebd285d-ca26-46b6-a846-4459e1b2af1e). The image analysis code is available upon request. Full details of the code are provided in the Materials and Methods section.

Expanded View for this article is available online.

Author contributions

Deniz Saltukoglu: Conceptualization; formal analysis; investigation; visualization; methodology; writing – original draft; project administration; writing – review and editing. **Bugra Özdemir:** Data curation; software; formal analysis; methodology; writing – review and editing. **Michael Holtmannspötter:** Data curation; investigation; writing – review and editing. **Ralf Reski:** Funding acquisition; writing – review and editing. **Jacob Piehler:** Resources; supervision; funding acquisition; writing – review and editing. **Rainer Kurre:** Resources; funding acquisition; investigation; writing – review and editing. **Michael Reth:** Conceptualization; resources; supervision; funding acquisition; writing – original draft; writing – review and editing.

Disclosure and competing interests statement

The authors declare that they have no conflict of interest.

References

Aspenström P (2014) BAR domain proteins regulate rho GTPase signaling. *Small GTPases* 5: 7

Becalska AN, Kelley CF, Berciu C, Stanishneva-Konovalova TB, Fu X, Wang S, Sokolova OS, Nicastro D, Rodal AA (2013) Formation of membrane ridges and scallops by the F-BAR protein nervous wreck. *Mol Biol Cell* 24: 2406–2418

Becker M, Hobeika E, Jumaa H, Reth M, Maity PC (2017) CXCR4 signaling and function require the expression of the IgD-class B-cell antigen receptor. *Proc Natl Acad Sci U S A* 114: 5231–5236

Bement WM, Leda M, Moe AM, Kita AM, Larson ME, Golding AE, Pfeuti C, Su K-C, Miller AL, Goryachev AB *et al* (2015) Activator-inhibitor coupling between rho signalling and Actin assembly makes the cell cortex an excitable medium. *Nat Cell Biol* 17: 1471–1483

Bouafia A, Lofek S, Bruneau J, Chentout L, Lamrini H, Trinquand A, Deau M-C, Heurtier L, Meignin V, Picard C *et al* (2019) Loss of ARHGEF1 causes a human primary antibody deficiency. *J Clin Invest* 129: 1047–1060

Cai E, Marchuk K, Beemiller P, Beppler C, Rubashkin MG, Weaver VM, Gérard A, Liu T-L, Chen B-C, Betzig E *et al* (2017) Visualizing dynamic microvillar search and stabilization during ligand detection by T cells. *Science* 356: eaal318

Carrasco YR, Batista FD (2007) B cells acquire particulate antigen in a macrophage-rich area at the boundary between the follicle and the subcapsular sinus of the lymph node. *Immunity* 27: 160–171

Chen B-C, Legant WR, Wang K, Shao L, Milkie DE, Davidson MW, Janetopoulos C, Wu XS, Hammer JA 3rd, Liu Z *et al* (2014) Lattice light-sheet microscopy: imaging molecules to embryos at high spatiotemporal resolution. *Science* 346: 1257998

Cinamon G, Zachariah MA, Lam OM, Foss FW Jr, Cyster JG (2008) Follicular shuttling of marginal zone B cells facilitates antigen transport. *Nat Immunol* 9: 54–62

Cyster JG (2010) B cell follicles and antigen encounters of the third kind. *Nat Immunol* 11: 989–996

Driscoll MK, Welf ES, Jamieson AR, Dean KM, Isogai T, Fiolka R, Danuser G (2019) Robust and automated detection of subcellular morphological motifs in 3D microscopy images. *Nat Methods* 16: 1037–1044

Fernandes RA, Ganzinger KA, Tzou JC, Jönsson P, Lee SF, Palayret M, Santos AM, Carr AR, Ponjavic A, Chang VT *et al* (2019) A cell topography-based mechanism for ligand discrimination by the T cell receptor. *Proc Natl Acad Sci U S A* 116: 14002–14010

Fernández-Segura E, García JM, López-Escámez JA, Campos A (1994) Surface expression and distribution of fc receptor III (CD16 molecule) on human natural killer cells and polymorphonuclear neutrophils. *Microsc Res Tech* 28: 277–285

Franke C, Chum T, Kvíčalová Z, Glatzová D, Gentsch GJ, Rodriguez A, Helmerich DA, Herdly L, Mavila H, Frank O *et al* (2022) Approach to map nanotopography of cell surface receptors. *Commun Biol* 5: 218

Fricke R, Gohl C, Dharmalingam E, Grevelhörster A, Zahedi B, Harden N, Kessels M, Qualmann B, Bogdan S (2009) Drosophila Cip4/Toca-1 integrates membrane trafficking and Actin dynamics through WASP and SCAR/WAVE. *Curr Biol* 19: 1429–1437

Ghosh S, Feigelson SW, Montresor A, Shimoni E, Roncato F, Legler DF, Laudanna C, Haran G, Alon R (2021) CCR7 signalosomes are preassembled on tips of lymphocyte microvilli in proximity to LFA-1. *Biophys J* 120: 4002–4012

Golub T, Caroni P (2005) PI(4,5)P2-dependent microdomain assemblies capture microtubules to promote and control leading edge motility. *J Cell Biol* 169: 151–165

Gonzalez SF, Degn SE, Pitcher LA, Woodruff M, Heesters BA, Carroll MC (2011) Trafficking of B cell antigen in lymph nodes. *Annu Rev Immunol* 29: 215–233

Hao J-J, Wang G, Pisitkun T, Patino-Lopez G, Nagashima K, Knepper MA, Shen R-F, Shaw S (2008) Enrichment of distinct microfilament-associated and GTP-binding-proteins in membrane/microvilli fractions from lymphoid cells. *J Proteome Res* 7: 2911–2927

He X, Kläsener K, Iype JM, Becker M, Maity PC, Cavallari M, Nielsen PJ, Yang J, Reth M (2018) Continuous signaling of CD79b and CD19 is required for the fitness of Burkitt lymphoma B cells. *EMBO J* 37: e97980

Ho H-YH, Rohatgi R, Lebensohn AM, Ma L, Li J, Gygi SP, Kirschner MW (2004) Toca-1 mediates Cdc42-dependent Actin nucleation by activating the N-WASP-WIP complex. *Cell* 118: 203–216

Isensee F, Jaeger PF, Kohl SAA, Petersen J, Maier-Hein KH (2021) nnU-net: a self-configuring method for deep learning-based biomedical image segmentation. *Nat Methods* 18: 203–211

Jerman T, Pernuš F, Likar B, Špiclin Ž (2016a) Blob enhancement and visualization for improved intracranial aneurysm detection. *IEEE Trans Vis Comput Graph* 22: 1705–1717

Jerman T, Pernus F, Likar B, Spiclin Z (2016b) Enhancement of vascular structures in 3D and 2D angiographic images. *IEEE Trans Med Imaging* 35: 2107–2118

Jung Y, Riven I, Feigelson SW, Kartvelishvily E, Tohya K, Miyasaka M, Alon R, Haran G (2016) Three-dimensional localization of T-cell receptors in relation to microvilli using a combination of superresolution microscopies. *Proc Natl Acad Sci U S A* 113: E5916−E5924

Jung Y, Wen L, Altman A, Ley K (2021) CD45 pre-exclusion from the tips of T cell microvilli prior to antigen recognition. *Nat Commun* 12: 3872

Junt T, Moseman EA, Iannacone M, Massberg S, Lang PA, Boes M, Fink K, Henrickson SE, Shayakhmetov DM, Di Paolo NC *et al* (2007) Subcapsular sinus macrophages in lymph nodes clear lymph-borne viruses and present them to antiviral B cells. *Nature* 450: 110−114

Kelley CF, Becalska AN, Berciu C, Nicastro D, Rodal AA (2015) Assembly of Actin filaments and microtubules in Nwk F-BAR-induced membrane deformations. *Commun Integr Biol* 8: e1000703

Keppler SJ, Burbage M, Gasparrini F, Hartjes L, Aggarwal S, Massaad MJ, Geha RS, Bruckbauer A, Batista FD (2018) The lack of WIP binding to Actin results in impaired B cell migration and altered humoral immune responses. *Cell Rep* 24: 619−629

Kläsener K, Maity PC, Hobeika E, Yang J, Reth M (2014) B cell activation involves nanoscale receptor reorganizations and inside-out signaling by Syk. *Elife* 3: e02069

Koch AJ, Meinhardt H (1994) Biological pattern formation: from basic mechanisms to complex structures. *Rev Mod Phys* 66: 1481−1507

Koenderink JJ, van Doorn AJ (1992) Surface shape and curvature scales. *Image Vis Comput* 10: 557−564

de Kreuk B-J, Hordijk PL (2012) Control of rho GTPase function by BAR-domains. *Small GTPases* 3: 45−52

Kuka M, Iannacone M (2018) Viral subversion of B cell responses within secondary lymphoid organs. *Nat Rev Immunol* 18: 255−265

Lanzi G, Moratto D, Vairo D, Masneri S, Delmonte O, Paganini T, Parolini S, Tabellini G, Mazza C, Savoldi G *et al* (2012) A novel primary human immunodeficiency due to deficiency in the WASP-interacting protein WIP. *J Exp Med* 209: 29−34

Lee TC, Kashyap RL, Chu CN (1994) Building skeleton models via 3-D medial surface axis thinning algorithms. *CVGIP: Graph Model Image Process* 56: 462−478

Liao P-S, Chen T-S, Chung P-C (2001) A fast algorithm for multilevel thresholding. *J Inf Sci Eng* 17: 713−727

Lillemeier BF, Mörtelmaier MA, Forstner MB, Huppa JB, Groves JT, Davis MM (2010) TCR and Lat are expressed on separate protein islands on T cell membranes and concatenate during activation. *Nat Immunol* 11: 90−96

Maity PC, Blount A, Jumaa H, Ronneberger O, Lillemeier BF, Reth M (2015) B cell antigen receptors of the IgM and IgD classes are clustered in different protein islands that are altered during B cell activation. *Sci Signal* 8: ra93

Majstoravich S, Zhang J, Nicholson-Dykstra S, Linder S, Friedrich W, Siminovitch KA, Higgs HN (2004) Lymphocyte microvilli are dynamic, actin-dependent structures that do not require Wiskott-Aldrich syndrome protein (WASp) for their morphology. *Blood* 104: 1396−1403

Mattila PK, Feest C, Depoil D, Treanor B, Montaner B, Otipoby KL, Carter R, Justement LB, Bruckbauer A, Batista FD (2013) The actin and tetraspanin networks organize receptor nanoclusters to regulate B cell receptor-mediated signaling. *Immunity* 38: 461−474

Mattila PK, Batista FD, Treanor B (2016) Dynamics of the actin cytoskeleton mediates receptor cross talk: an emerging concept in tuning receptor signaling. *J Cell Biol* 212: 267−280

McDonald NA, Gould KL (2016) Linking up at the BAR: oligomerization and F-BAR protein function. *Cell Cycle* 15: 1977−1985

Michaud A, Leda M, Swider ZT, Kim S, He J, Landino J, Valley JR, Huisken J, Goryachev AB, von Dassow G *et al* (2022) A versatile cortical pattern-forming circuit based on rho, F-actin, Ect2, and RGA-3/4. *J Cell Biol* 221: e202203017

Miki H, Yamaguchi H, Suetsugu S, Takenawa T (2000) IRSp53 is an essential intermediate between Rac and WAVE in the regulation of membrane ruffling. *Nature* 408: 732−735

Moshous D, Martin E, Carpentier W, Lim A, Callebaut I, Canioni D, Hauck F, Majewski J, Schwartzentruber J, Nitschke P *et al* (2013) Whole-exome sequencing identifies Coronin-1A deficiency in 3 siblings with immunodeficiency and EBV-associated B-cell lymphoproliferation. *J Allergy Clin Immunol* 131: 1594−1603

Niblack W (1985) *An introduction to digital image processing*. København: Strandberg Publishing Company

Obino D, Farina F, Malbec O, Sáez PJ, Maurin M, Gaillard J, Dingli F, Loew D, Gautreau A, Yuseff M-I *et al* (2016) Actin nucleation at the centrosome controls lymphocyte polarity. *Nat Commun* 7: 10969

Orbach R, Su X (2020) Surfing on membrane waves: microvilli, curved membranes, and immune signaling. *Front Immunol* 11: 2187

Otsu N (1979) A threshold selection method from gray-level histograms. *IEEE Trans Syst Man Cybern* 9: 62−66

Phan TG, Grigorova I, Okada T, Cyster JG (2007) Subcapsular encounter and complement-dependent transport of immune complexes by lymph node B cells. *Nat Immunol* 8: 992−1000

Pineau J, Pinon L, Mesdjian O, Fattaccioli J, Lennon Duménil A-M, Pierobon P (2022) Microtubules restrict F-Actin polymerization to the immune synapse via GEF-H1 to maintain polarity in lymphocytes. *Elife* 11: e78330

Qi H, Egen JG, Huang AYC, Germain RN (2006) Extrafollicular activation of lymph node B cells by antigen-bearing dendritic cells. *Science* 312: 1672−1676

Rey-Suarez I, Wheatley BA, Koo P, Bhanja A, Shu Z, Mochrie S, Song W, Shroff H, Upadhyaya A (2020) WASP family proteins regulate the mobility of the B cell receptor during signaling activation. *Nat Commun* 11: 439

Roh K-H, Lillemeier BF, Wang F, Davis MM (2015) The coreceptor CD4 is expressed in distinct nanoclusters and does not colocalize with T-cell receptor and active protein tyrosine kinase p56lck. *Proc Natl Acad Sci U S A* 112: E1604−E1613

Roozendaal R, Mebius RE, Kraal G (2008) The conduit system of the lymph node. *Int Immunol* 20: 1483−1487

Roozendaal R, Mempel TR, Pitcher LA, Gonzalez SF, Verschoor A, Mebius RE, von Andrian UH, Carroll MC (2009) Conduits mediate transport of low-molecular-weight antigen to lymph node follicles. *Immunity* 30: 264−276

Saarikangas J, Kourdougli N, Senju Y, Chazal G, Segerstråle M, Minkeviciene R, Kuurne J, Mattila PK, Garrett L, Hölter SM *et al* (2015) MIM-induced membrane bending promotes dendritic spine initiation. *Dev Cell* 33: 644−659

Saengsawang W, Taylor KL, Lumbard DC, Mitok K, Price A, Pietila L, Gomez TM, Dent EW (2013) CIP4 Coordinates with phospholipids and Actin-associated proteins to localize to the protruding edge and produce Actin ribs and veils. *J Cell Sci* 126: 2411−2423

Sage PT, Varghese LM, Martinelli R, Sciuto TE, Kamei M, Dvorak AM, Springer TA, Sharpe AH, Carman CV (2012) Antigen recognition is facilitated by invadosome-like protrusions formed by memory/effector T cells. *J Immunol* 188: 3686−3699

Sanjaya YC, Gunawan AAS, Irwansyah E (2020) Semantic segmentation for aerial images: a literature review. *EMACS J* 2: 133−139

Sato Y, Nakajima S, Shiraga N, Atsumi H, Yoshida S, Koller T, Gerig G, Kikinis R (1998) Three-dimensional multi-scale line filter for segmentation and

visualization of curvilinear structures in medical images. *Med Image Anal* 2: 143–168

Schnyder T, Castello A, Feest C, Harwood NE, Oellerich T, Urlaub H, Engelke M, Wienands J, Bruckbauer A, Batista FD (2011) B cell receptor-mediated antigen gathering requires ubiquitin ligase Cbl and adaptors Grb2 and Dok-3 to recruit dynein to the signaling microcluster. *Immunity* 34: 905–918

Simunovic M, Šarić A, Henderson JM, Lee KYC, Voth GA (2017) Long-range organization of membrane-curving proteins. *ACS Cent Sci* 3: 1246–1253

Sofroniew N, Lambert T, Evans K, Nunez-Iglesias J, Bokota G, Peña-Castellanos G, Winston P, Yamauchi K, Bussonnier M, Pop DD *et al* (2021) napari/napari: 0.4.12rc1. *Zenodo* https://doi.org/10.5281/zenodo.5586292

Suetsugu S, Gautreau A (2012) Synergistic BAR-NPF interactions in actin-driven membrane remodeling. *Trends Cell Biol* 22: 141–150

Suetsugu S, Kurisu S, Takenawa T (2014) Dynamic shaping of cellular membranes by phospholipids and membrane-deforming proteins. *Physiol Rev* 94: 1219–1248

Sugiyama T, Pramanik MK, Yumura S (2015) Microtubule-mediated inositol lipid signaling plays critical roles in regulation of Blebbing. *PLoS One* 10: e0137032

Sullivan C, Kaszynski A (2019) PyVista: 3D plotting and mesh analysis through a streamlined interface for the Visualization Toolkit (VTK). *J Open Source Softw* 4: 1450

Suzuki K, Grigorova I, Phan TG, Kelly LM, Cyster JG (2009) Visualizing B cell capture of cognate antigen from follicular dendritic cells. *J Exp Med* 206: 1485–1493

Thrasher AJ (2009) New insights into the biology of Wiskott-Aldrich syndrome (WAS). *ASH Educ Prog Book* 1: 132–138

Tolar P (2017) Cytoskeletal control of B cell responses to antigens. *Nat Rev Immunol* 17: 621–634

Treanor B, Depoil D, Gonzalez-Granja A, Barral P, Weber M, Dushek O, Bruckbauer A, Batista FD (2010) The membrane skeleton controls diffusion dynamics and signaling through the B cell receptor. *Immunity* 32: 187–199

Tversky A (1977) Features of similarity. *Psychol Rev* 84: 327–352

Weems AD, Welf ES, Driscoll MK, Mazloom-Farsibaf H, Chang B-J, Weiss BG, Chi J, Dean KM, Fiolka R, Danuser G (2021) Blebs promote cell survival by assembling oncogenic signaling hubs. *bioRxiv* https://doi.org/10.1101/2021.04.23.441200 [PREPRINT]

Wu Z, Su M, Tong C, Wu M, Liu J (2018) Membrane shape-mediated wave propagation of cortical protein dynamics. *Nat Commun* 9: 136

Wykes M, Pombo A, Jenkins C, MacPherson GG (1998) Dendritic cells interact directly with naive B lymphocytes to transfer antigen and initiate class switching in a primary T-dependent response. *J Immunol* 161: 1313–1319

Xiong D, Xiao S, Guo S, Lin Q, Nakatsu F, Wu M (2016) Frequency and amplitude control of cortical oscillations by phosphoinositide waves. *Nat Chem Biol* 12: 159–166

Zhao H, Michelot A, Koskela EV, Tkach V, Stamou D, Drubin DG, Lappalainen P (2013) Membrane-sculpting BAR domains generate stable lipid microdomains. *Cell Rep* 4: 1213–1223

Zhao J, Ai D, Yang Y, Song H, Huang Y, Wang Y, Yang J (2019) Deep feature regression (DFR) for 3D vessel segmentation. *Phys Med Biol* 64: 115006